

AD-A259 944



2

240600-4-F

Final Report

SAXON-FPN NAWC/ERIM P-3 SAR DATA DISTRIBUTION AND ANALYSIS

C.C.WACKERMAN
Center for Earth Sciences
Advanced Concepts Division

NOVEMBER 1992

DTIC
SELECTE
JAN 25 1993
S B D

Office of Naval Research
800 N. Quincy
Arlington, VA 22217
Contract No.: N00014-91-C-0207
Technical Monitor: Frank Herr

Original contains color
plates: All DTIC reproductions
will be in black and
white.

DISTRIBUTION STATEMENT A
Approved for public release
Distribution Unlimited

93-01240



6488



P.O. Box 134001
Ann Arbor, MI 48113-4001

93 I 22 097

240600

Contract Number: N00014-91-C-0207

Final Report:

External:

Frank L. Herr
Scientific Officer
Office of Naval Research
800 N. Quincy Street
Attn: FLH Code 1121RS
Arlington VA 22217-5000
(1)

DCMAO, Detroit
ATTN: ACO
Contract Number: N00014-91-C-0207
McNamara Federal Building
477 Michigan Avenue
Detroit Michigan 48226-2506
(1)

Naval Research Laboratory
Director
Code 2627
Washington DC 20375
(1)

DTIC - 2

Internal:

IRC - 1
Repro - 1
C. Wackerman - 3
Marsha Neagle - original

REPORT DOCUMENTATION PAGE				Form Approved OMB No. 0704-0188	
1a REPORT SECURITY CLASSIFICATION Unclassified		1b RESTRICTIVE MARKINGS			
2a SECURITY CLASSIFICATION AUTHORITY		3 DISTRIBUTION/AVAILABILITY OF REPORT Unlimited			
2b DECLASSIFICATION/DOWNGRADING SCHEDULE					
4 PERFORMING ORGANIZATION REPORT NUMBER(S) 240600-4-F		5 MONITORING ORGANIZATION REPORT NUMBER(S)			
6a NAME OF PERFORMING ORGANIZATION Environmental Research Institute of Michigan		6b OFFICE SYMBOL <i>(if applicable)</i>	7a NAME OF MONITORING ORGANIZATION ONR		
6c ADDRESS (City, State, and ZIP Code) P.O. Box 134001 Ann Arbor, MI 48113-4001		7b ADDRESS (City, State, and ZIP Code) Arlington, VA 22217-5000			
8a NAME OF FUNDING /SPONSORING ORGANIZATION ONR		8b OFFICE SYMBOL <i>(if applicable)</i>	9. PROCUREMENT INSTRUMENT IDENTIFICATION NUMBER		
8c ADDRESS (City, State, and ZIP Code) Arlington, VA 22217-5000		10. SOURCE OF FUNDING NUMBERS			
		PROGRAM ELEMENT NO.	PROJECT NO.	TASK NO.	WORK UNIT ACCESSION NO.
11 TITLE (Include Security Classification) SAXON-FPN NAWC/ERIM P-3 SAR Data Distribution and Analysis					
12. PERSONAL AUTHOR(S) Christopher C. Wackerman					
13a TYPE OF REPORT Final		13b. TIME COVERED FROM 10/91 TO 9/92	14. DATE OF REPORT (Year, Month, Day) 1992 November 1		15. PAGE COUNT 63
16 SUPPLEMENTARY NOTATION					
17. COSATI CODES			18. SUBJECT TERMS <i>(Continue on reverse if necessary and identify by block number)</i> SAR, Spotlight Mode, Modulation Transfer Function		
FIELD	GROUP	SUB-GROUP			
19 ABSTRACT <i>(Continue on reverse if necessary and identify by block number)</i> As part of the SAXON-FPN Experiment, ERIM collected, processed and distributed SAR imagery from the ERIM/NAWC P-3 system. In addition we analyzed data collected in a spotlight mode to extract estimates of the real modulation transfer function. The report summarizes both activities, along with an analysis of the cross-channel coupling for cross-polarized data for the system.					
20 DISTRIBUTION/AVAILABILITY OF ABSTRACT <input type="checkbox"/> UNCLASSIFIED/UNLIMITED <input type="checkbox"/> SAME AS RPT. <input type="checkbox"/> DTIC USERS			21. ABSTRACT SECURITY CLASSIFICATION Unclassified		
22a NAME OF RESPONSIBLE INDIVIDUAL C.C. Wackerman		22b TELEPHONE (Include Area Code) (313) 994-1200		22c OFFICE SYMBOL	

CONTENTS

FIGURES v

TABLESvii

1.0 INTRODUCTION AND SUMMARY 1

2.0 SAR IMAGE GENERATION AND DISTRIBUTION 3

3.0 ESTIMATION OF THE CROSS-CHANNEL COUPLING 8

4.0 SPOTLIGHT DATA ANALYSIS 16

 4.1 PROCESSING SPOTLIGHT SAR DATA 17

 4.2 GENERATING THREE-DIMENSIONAL
 FOURIER TRANSFORMS 20

 4.3 ESTIMATING MTF PARAMETERS FROM THE
 SPOTLIGHT DATA 43

 4.4 COMPARISON TO IN-SITU MEASUREMENTS 52

5.0 REFERENCES 54

APPENDIX: ESTIMATION OF 3-D OCEAN WAVE SPECTRA
 FROM SPOTLIGHT SAR DATA DURING SAXON-FPN 55

DTIC QUALITY INSPECTED 5

Accession For	
NTIS GRA&I	<input checked="" type="checkbox"/>
DTIC TAB	<input type="checkbox"/>
Unannounced	<input type="checkbox"/>
Justification	
By _____	
Distribution/	
Availability Codes	
Dist	Avail and/or Special
A-1	

FIGURES

1.	Clutter to Noise Ratios for the VV and VH Channels for an X-Band Polarimetric Collection	10
2.	Clutter to Noise Ratios for the HH and HV Channels for an X-Band Polarimetric Collection	11
3.	Correlation Between the Like- and Cross-Polarized Channels for VH	12
4.	Correlation Between the Like- and Cross-Polarized Channels for HV	13
5.	Coupling Between the HV Channel and the Like-Polarized Channels	14
6.	Coupling Between the VH Channel and the Like-Polarized Channels	15
7.	Schematic Illustrating How Spotlight Data was Processed for This Analysis	18
8.	Schematic Illustrating How Three-Dimensional Fourier Transforms are Generated From Spotlight Imagery	22
9.	Flowchart Showing the Algorithm, With Corrections, for Generating Three-Dimensional Fourier Transform Data	25
10.	Example of Spotlight Imagery From Nov. 6 Pass 8. Every Other Image is Shown	27
11.	Example of Image Spectra From Nov. 6 Pass 8. Spectra are Highly Saturated to Illustrate the MTF and IPR Spectral Weightings. Every Other Spectra is Shown	29
12.	Contour Plots of Dominant Wave Peaks in Spotlight Spectra From Nov. 6 Pass 8. Every Other Spectra is Shown	32

FIGURES (Continued)

13.	Contour Plots of Dominant Wave Peaks in Spotlight Spectra From Nov. 6 pass 14. Every Other Spectra is Shown	33
14.	Dominant Wave Length and Wave Direction Versus Look Angle (i.e. Squint Angle) for Nov. 6 Pass 8 Spotlight Data	34
15.	Dominant Wave Length and Wave Direction Versus Look Angle (i.e. Squint Angle) for Nov. 6 Pass 14 Spotlight Data	35
16.	Average Spectral Intensity and Maximum Spectral Intensity for Nov. 6 Pass 8 Spotlight Data	36
17.	Average Spectral Intensity and Maximum Spectral Intensity for Nov. 6 Pass 14 Spotlight Data	37
18.	Three-Dimensional Fourier Transform of Nov. 6 Pass 8 Spotlight Data Collapsed into a Series of w vs. k Plots. Bars Indicate Ranges of k Values for a Given w Sample	39
19.	Three-Dimensional Fourier Transform of Nov. 6 Pass 8 Spotlight Data Shows 16 w Planes. Green Values Indicate Spectral Energy, Red Dot Indicates Dispersion Relation for Range Travelling Waves	41
20.	Three-Dimensional Fourier Transform of Nov. 6 Pass 14 Spotlight Data Collapsed Into a Series of w vs. k Plots. Bars Indicate Range if k Values for a Given w Sample	44
21.	Schematic Illustrating How Weighting on Image Spectra Versus Time Causes Smearing in Three-Dimensional Fourier Data	45
22.	Schematic Showing How Rotation of MTF Determines the Weighting of the Intensity of Image Spectra Versus Time	47
23.	Magnitude of SAR Image Spectra Versus Squint Angle (i.e. Time) for Nov. 6 Passes 14 and 28	49

FIGURES (Concluded)

24. Fit of SAR Data in Figure 23 to Linear MTF Model Across
Full Squint Angle Range 51

25. Fit of SAR Data in Figure 23 to Linear MTF Only Over Squint
Angle Ranges for Which the Velocity Bunching Term is Less
Than 0.5 53

TABLES

1. Processed SAR Stripmap Imagery 4

1.0 INTRODUCTION AND SUMMARY

Under this program, four main research activities were performed: (1) processing and distribution of SAR data collected with the airborne NAWC/ERIM P-3 Synthetic Aperture Radar (SAR) system; (2) determination of the cross-channel coupling in the cross-polarized data collected by the system; (3) generation of three-dimensional Fourier transforms from spotlight SAR data collected with the system and comparison with a linear Modulation Transfer Function (MTF) theory; and (4) generation of simulated SAR image spectrum using a non-linear MTF theory. The first three activities will be summarized in this report. The fourth activity is summarized in a second report [1].

The processing and distribution of SAR imagery is discussed in Section 2 where details on the image parameters and a summary of all the available data will be found. In total, 273 stripmap images, 64 spotlight images and 9 corrected spectra were generated and distributed.

The analysis of the cross-channel coupling in the system showed that the cross-polarized data was not useable; the coupling from the like-polarized channels swamped any actual cross-polarized return. This is discussed in Section 3.

Analysis of the spotlight data showed that a three-dimensional Fourier transform of the spotlight imagery did indicate a dispersion relation that was consistent with deep water wave dispersion. However it also indicated a large amount of smearing in the spectral domain. One dominant cause of the smearing is the SAR MTF, and it was shown that a plot of the SAR image spectrum as a function of time during the spotlight collection could be used to compare against models for the MTF while being invariant to registration errors in the data; registration errors being the other major cause of smearing in the spectral domain. Using a linear model, estimates for the three unknown parameters (the standard deviation of radial velocities, the magnitude of the

real transfer function, and the phase of the real transfer function) were generated from the SAR data. These estimates were not very tight due to both the noise in the SAR measurements as well as its general insensitivity to changes in the parameters, but they were sufficient to indicate intervals for the parameters. This is discussed in Section 4.

2.0 SAR IMAGE GENERATION AND DISTRIBUTION

Table 1 lists the SAR stripmap data that was generated from the NAWC/ERIM P-3 SAR system. This system is an airborne SAR, based in a P-3 aircraft. It has three frequencies, X-band (0.032 meters), C-band (0.0565 meters) and L-band, (0.2397 meters), and collects data in HH (horizontal transmit, horizontal receive), VV (vertical transmit, vertical receive) polarizations as well as cross-polarizations. As discussed in Section 3, the cross-polarized channels did not have sufficient signal to noise to be useful for the SAXON-FPN collection. For any one pass with the sensor, four channels can be recorded simultaneously where each channel can be any one of the possible wavelength/polarization combinations. The SAR imaging geometry parameters used for each image as well as the wavelength and polarization are recorded in Table 1.

The sensor normally collects data spaced at 1.2 meters in the slant range plane and 0.09 meters in the azimuth direction. The azimuth data is downsampled by a factor of 6 on the sensor to generate 0.54 meters samples. When the data is processed into an image, in order to generate imagery that covers more area, the data for the sensor is downsampled an additional three times, resulting in samples that are spaced by 1.62 meters in azimuth. This data is then coherently processed to generate a complex-valued SAR image. The image data is formed by taking the intensity of the complex-valued samples and averaging four intensity samples in range and three intensity samples in azimuth together to form one output sample. The output SAR imagery thus has a spacing of 4.8 meters in range and 4.86 meters in azimuth and is approximately 12 looks. The imagery was also mapped into the ground plane, and both slant plane and ground plane images are available for the data in Table 1.

Spotlight images were also processed for two passes; Nov. 6 pass 14 and Nov. 6 pass 28. Thirty-two images were generated for each pass spaced approximately every two degrees in squint angle. Each image was processed with an integration time of 1.5

TABLE 1.
PROCESSED SAR STRIPMAP IMAGERY

DATE	PASS	AIRCRAFT TRACK (°T)	AIRCRAFT ALTITUDE (FT)	AIRCRAFT SPEED (KTS)	WAVELENGTH/ POLARIZATION
Nov 6	2	330	5516	250.5	XVV, CVV, LVV, LHH
Nov 6	4	150	5516	243.0	XVV, CVV, LVV, LHH
Nov 6	5	240	5516	239.3	XVV, CVV, LVV, LHH
Nov 6	9	195	5573	246.6	XVV, CVV, LVV, LHH
Nov 6	10	285	5547	234.8	XVV, CVV, LVV, LHH
Nov 6	11	105	10269	244.0	XVV, CVV, LVV, LHH
Nov 6	12	240	10261	259.0	XVV, CVV, LVV, LHH
Nov 6	15	195	10277	265.8	XVV, CVV, LVV, LHH
Nov 6	16	330	10277	227.5	XVV, CVV, LVV, LHH
Nov 6	19	150	10292	241.1	XVV, CVV, LVV, LHH
Nov 6	21	285	20310	260.2	CVV, CHH, LVV, LHH
Nov 6	24	330	20341	245.8	CVV, CHH, LVV, LHH
Nov 6	25	150	20341	248.8	CVV, CHH, LVV, LHH
Nov 6	26	015	20341	251.7	CVV, CHH, LVV, LHH
Nov 6	29	240	20357	259.6	CVV, CHH, LVV, LHH
Nov 8	2	330	5122	257.0	XVV, CVV, LVV, LHH
Nov 8	4-7	150	5153	244.0	XVV, CVV, LVV, LHH
Nov 8	8-9	015	5161	252.0	XVV, CVV, LVV, LHH
Nov 8	10	240	5169	245.2	XVV, CVV, LVV, LHH
Nov 8	11	060	5201	240.0	XVV, CVV, LVV, LHH
Nov 8	12	285	5193	247.2	XVV, CVV, LVV, LHH
Nov 8	15	330	10426	247.2	XVV, CVV, LVV, LHH
Nov 8	16	150	10434	240.0	XVV, CVV, LVV, LHH
Nov 8	17	015	10450	244.1	XVV, CVV, LVV, LHH
Nov 8	18	240	10434	243.1	XVV, CVV, LVV, LHH
Nov 8	19	060	10450	245.9	XVV, CVV, LVV, LHH
Nov 8	20	285	10418	233.9	XVV, CVV, LVV, LHH
Nov 8	23	015	20530	251.9	CVV, CHH, LVV, LHH
Nov 8	24	240	20506	244.3	CVV, CHH, LVV, LHH

TABLE 1.
PROCESSED SAR STRIPMAP IMAGERY (CONTINUED)

DATE	PASS	AIRCRAFT TRACK (°T)	AIRCRAFT ALTITUDE (FT)	AIRCRAFT SPEED (KTS)	WAVELENGTH/ POLARIZATION
Nov 8	25	105	20530	251.2	CVV,CHH,LVV,LHH
Nov 8	26	240	20506	241.9	CVV,CHH,LVV,LHH
Nov 8	27	330	20530	239.4	CVV,CHH,LVV,LHH
Nov 8	28	150	20514	240.0	CVV,CHH,LVV,LHH
Nov 8	31	074	20467	264.5	CVV,CHH,LVV,LHH
Nov 8	32	180	20436	265.2	CVV,CHH,LVV,LHH
Nov 14	2	360	7917	269.0	XVV, CVV, LVV, LHH
Nov 15	1	360	8484	277.0	XVV, CVV, LVV, LHH
Nov 15	9	015	5201	278.5	XVV, XHH, CVV, CHH
Nov 15	14	240	5216	275.2	XVV, XHH, CVV, CHH
Nov 15	15	060	5201	296.5	XVV, XHH, CVV, CHH
Nov 19	2	135	4980	252.0	XVV, CVV, LVV, LHH
Nov 19	4	315	5060	252.0	XVV, CVV, LVV, LHH
Nov 19	7	045	4906	256.0	XVV, CVV, LVV, LHH
Nov 19	9	225	5000	245.5	XVV, CVV, LVV, LHH
Nov 19	13	135	18950	255.0	CVV, CHH, LVV, LHH
Nov 19	14	315	19450	244.6	CVV, CHH, LVV, LHH
Nov 19	16	045	19010	252.0	CVV, CHH, LVV, LHH
Nov 19	17	225	19130	248.6	CVV, CHH, LVV, LHH
Nov 19	21	000	4460	256.0	XVV, CVV, LVV, LHH
Nov 20	2	360	4870	260.0	LVV, LHH
Nov 26	2	360	11802	251.5	LVV, LHH
Nov 26	3	240	19340	242.5	CVV, CHH, LVV, LHH
Nov 26	6	015	19380	252.0	CVV, CHH, LVV, LHH
Nov 26	8	330	19349	255.9	CVV, CHH, LVV, LHH
Nov 26	10	150	19349	244.0	CVV, CHH, LVV, LHH
Nov 26	11	285	19400	251.0	CVV, CHH, LVV, LHH
Nov 26	13	150	10481	255.0	XVV, CVV, LVV, LHH
Nov 26	14	330	10560	248.6	XVV, CVV, LVV, LHH

TABLE 1.
PROCESSED SAR STRIPMAP IMAGERY (CONCLUDED)

DATE	PASS	AIRCRAFT TRACK (°T)	AIRCRAFT ALTITUDE (FT)	AIRCRAFT SPEED (KTS)	WAVELENGTH/ POLARIZATION
Nov 27	2	360	4870	253.9	XVV,XHH,CVV,LHH
Nov 27	6	345	4980	249.9	XVV,XHH,CVV,LHH
Nov 27	9	255	4870	270.3	XVV,XHH,CVV,LHH
Nov 27	22	345	19743	252.7	XVV,XHH,CVV,LHH
Nov 27	26	255	19759	249.7	XVV,XHH,CVV,LHH
Nov 27	28	300	9852	251.4	XVV,XHH,CVV,LHH
Nov 27	30	345	9978	257.2	XVV,XHH,CVV,LHH

seconds. For spotlight data no downsampling is done by either the sensor or the processor so the complex-valued image samples are spaced by 1.2 meters in the range direction and 0.09 meters in the azimuth direction. Two intensity values in range and 27 intensity values in azimuth are then averaged together to generate images with 2.4 meter samples in range and 2.43 meter samples in azimuth.

A series of stripmap images processed at different integration times was also generated from two passes; Nov. 6 pass 25 and Nov. 26 pass 3. Only the L-band VV data was used and the integration times were set at 0.012, 0.1, 0.2, 0.3, 0.4, 0.5, 0.6, 0.7, 0.8, 0.9 and 1.0 seconds; the lowest value being the smallest possible integration time since it is the time it took the sensor to fly one azimuth sample.

Finally, spectra were generated from a small subset of the stripmap and spotlight data that were corrected for the sensor Impulse Point Response (IPR) weighting; Nov. 15 pass 14 and Nov. 6 passes 2, 19 and 25. The correction procedure used can be found in [2]. If we let i represent the complex-valued SAR image and $FT[\]$ represent the Fourier transform of what is within the brackets, then the correction procedure is

$$S = \frac{|FT[|i|^2]|^2}{|FT^{-1}[FT[i]^2]|^2} \quad (1)$$

where S is the estimated spectrum. The numerator in Eq. (1) is the normal image spectrum. The denominator in Eq. (1) represents an estimate of the SAR IPR weighting which is then removed from the image spectrum by division.

3.0 ESTIMATION OF THE CROSS-CHANNEL COUPLING

One of the intended uses for the P-3 SAR data was to compare with cross-polarization data collected *in situ*. Before this comparison could be done, we analyzed the cross-polarization data collected by the P-3 SAR to determine whether it contained useful data. The cross-polarized data was collected with X-band and C-band, for which the signal to noise ratio over the ocean is lower, and thus had the potential to be corrupted by leakage from the like-polarized channels.

We assumed that

$$d_{VH} = p_1 r_{VV} + p_2 r_{HH} + r_{VH} \quad (2)$$

where d_{VH} is the complex-valued data recorded by the sensor in the VH channel, r_{VV} is the complex-valued VV response from the target, r_{HH} is the complex-valued HH response, and r_{VH} is the cross-polarized response. The constants p_1 and p_2 represent the cross-channel couplings; i.e. the amount of leakage from the like-polarized return into the cross-polarized channel. To estimate these couplings we assume that $E[r_{VH} r_{VV}^*] = E[r_{VH} r_{HH}^*] = 0$ where $E[\]$ represents the expected value (over a large number of image samples) of what is within the brackets. This assumes that the like and cross-channels are uncorrelated. Using Eq. (2) we have that

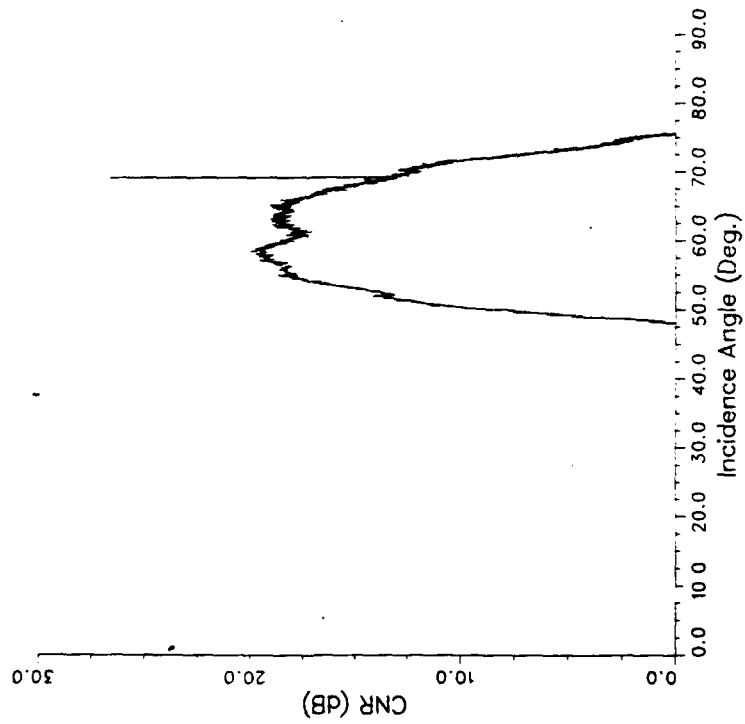
$$\begin{aligned} E[d_{VH} r_{VV}^*] &= p_1 E[|r_{VV}|^2] + p_2 E[r_{HH} r_{VV}^*] \\ E[d_{VH} r_{HH}^*] &= p_1 E[r_{VV} r_{HH}^*] + p_2 E[|r_{HH}|^2] \end{aligned} \quad (3)$$

All of the $E[\]$ quantities in Eq. (3) can be measured. Using these quantities as coefficients, the linear equations in Eq. (3) can then be solved for p_1 and p_2 . In general we would expect these couplings to be a function of incidence angle, and thus Eq. (3) needs to be solved for each incidence angle. A similar set of equations can be generated for the HV channel.

Figure 1 shows the clutter to noise ratio for the VV and VH channels for X-band data collected at the lowest altitude (5000 feet) and the highest wind speed, and thus with the best chance of having useful cross-polarized data. Note that the cross-polarized channel is approximately 15 dB down from the like-polarized channel indicating that the coupling between the channels must be less than 15 dB if the cross-polarized data is to be useful. Figure 2 shows the same curves for the HH and HV changes; note the expected decrease in clutter to noise ratio between VV and HH, although the cross-polarized return is only 5 dB down from the like-polarized return for this case. The cross-channel correlation (i.e. the left hand side of Eq. (3)) is shown in Figure 3 for the VH channel and in Figure 4 for the HV channel. Using these with the data in Figures 1 and 2 generates the estimates of p_1 and p_2 shown in Figure 5 for the HV channel and in Figure 6 for the VH channel. At the location of the peak in clutter to noise for Figures 1 and 2 (approximately 60 degrees incidence angle), the HV coupling with the VV channel is approximately -20 dB and with the HH channel is approximately -10 dB; borderline values for useful data. The VH coupling is similar; 1-18 dB for the V channel and -10 dB for the H channel.

Using the values in Figures 5 and 6, we can correct the cross-polarized data by subtracting out the coupling from the like-polarized channels. When we performed this for the data being analyzed, the resulting cross-polarized channels were only noise; i.e. no useful data was left. This indicated that the cross-polarized data was being dominated by the leakage from the like channels and not from actual cross-polarized returns from the ocean surface. Since this was the lowest altitude data, and the highest wind speed, it was the most favorable. We therefore concluded that the cross-polarized data from the experiment was not useful.

Clutter To Noise Ratio
VV Channel



Clutter To Noise Ratio
VH Channel

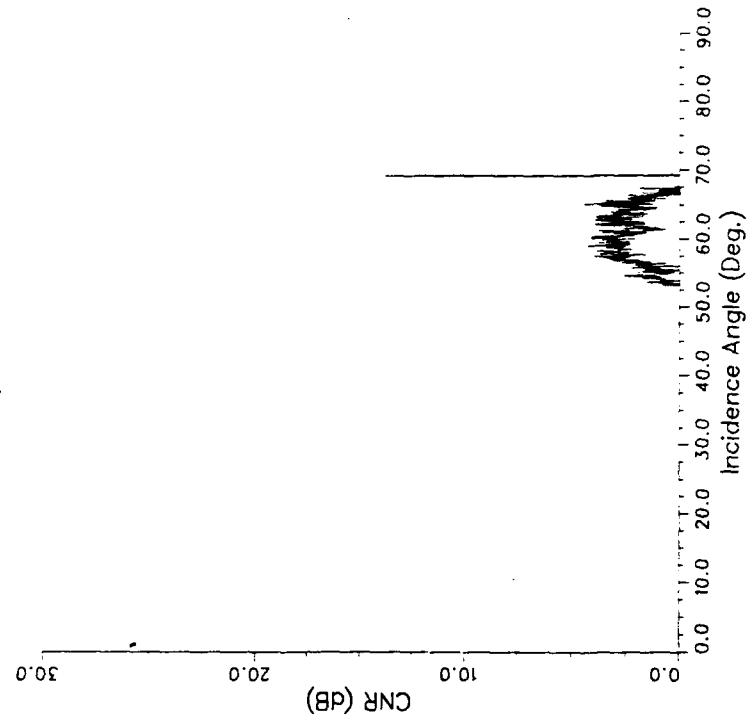
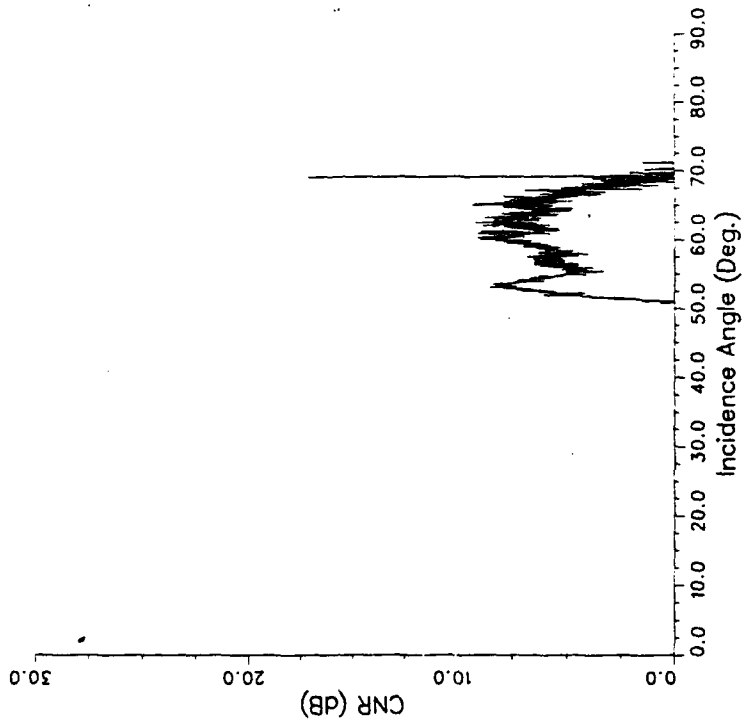


Figure 1. Clutter to Noise Ratios for the VV and VH Channels for an X-Band Polarimetric Collection.

Clutter To Noise Ratio
HH Channel



Clutter To Noise Ratio
HV Channel

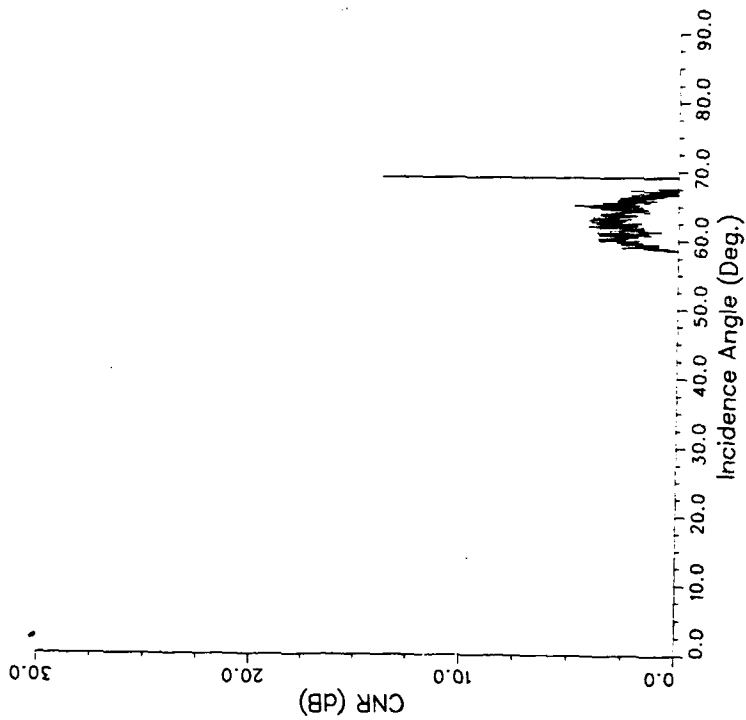


Figure 2. Clutter to Noise Ratios for the HH and HV Channels for an X-Band Polarimetric Collection.

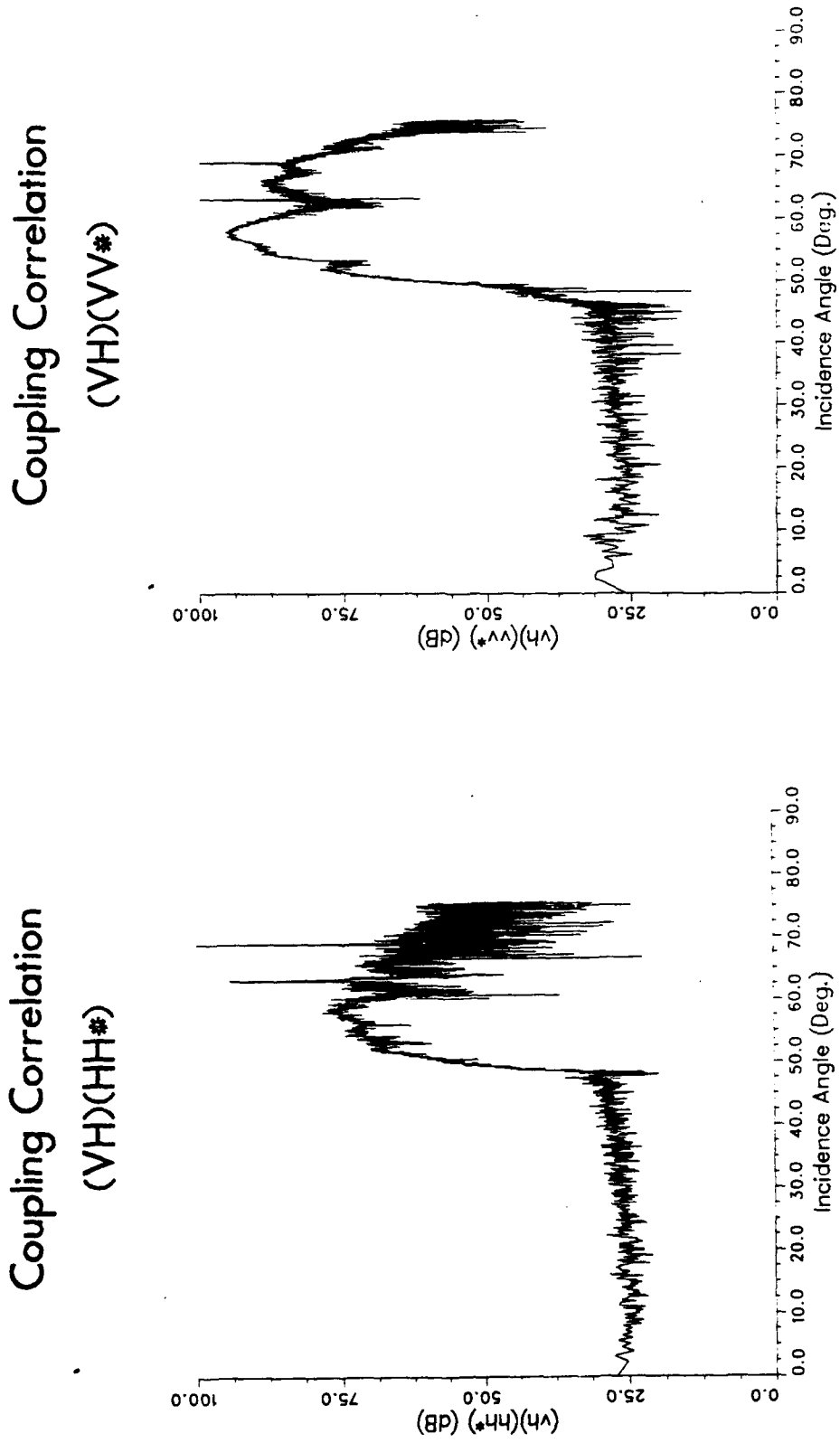
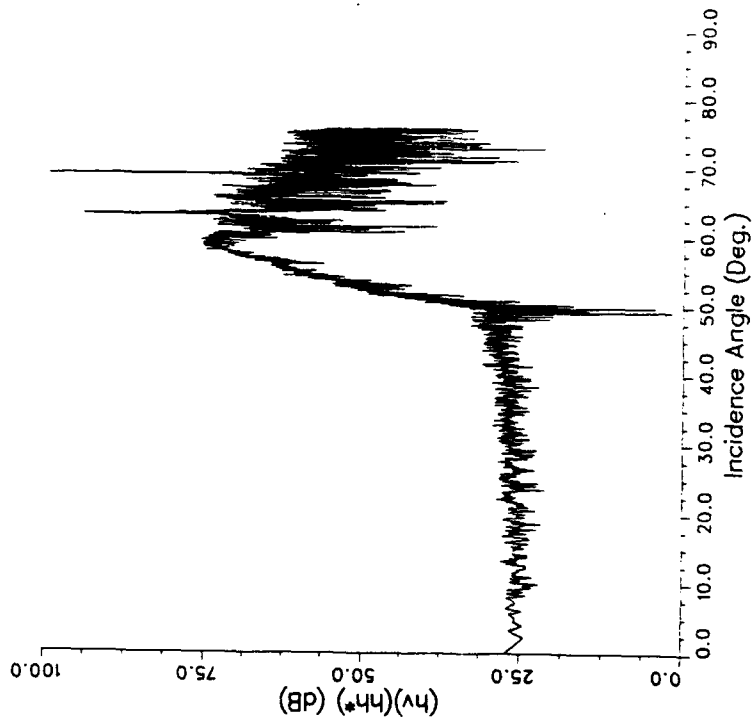


Figure 3. Correlation Between the Like- and Cross-Polarized Channels for VH.

Coupling Correlation
(HV)(HH*)



Coupling Correlation
(HV)(VV*)

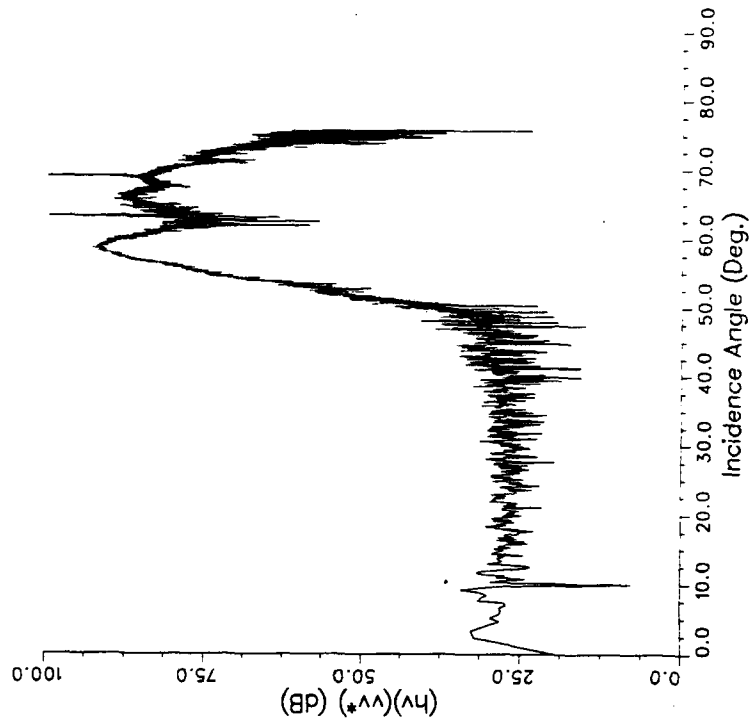
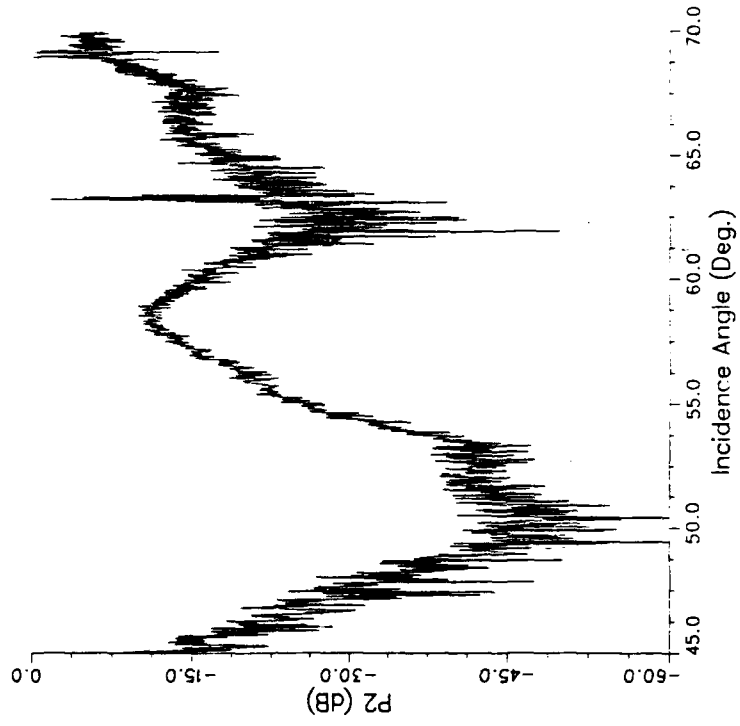


Figure 4. Correlation Between the Like- and Cross-Polarized Channels for HV.

Coupling Scale P2

HV Channel



Coupling Scale P1

HV Channel

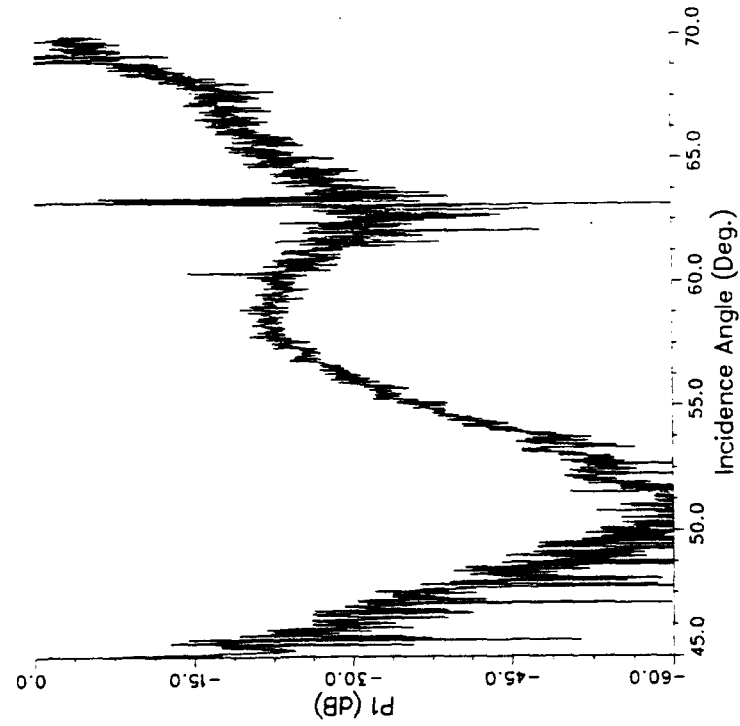


Figure 5. Coupling Between the HV Channel and the Like-Polarized Channels.

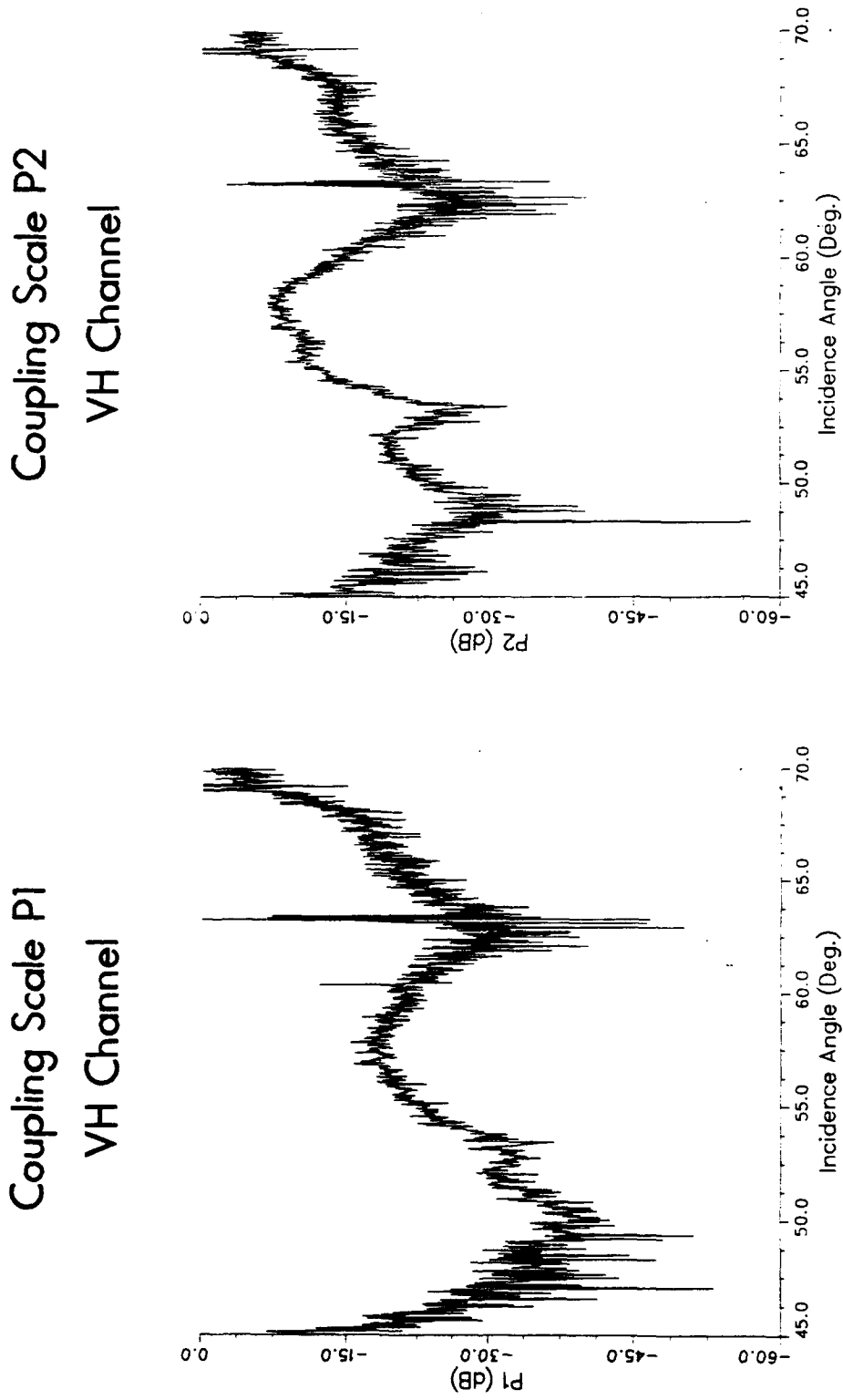


Figure 6. Coupling Between the VH Channel and the Like-Polarized Channels.

4.0 SPOTLIGHT DATA ANALYSIS

The major analysis task for this program was to utilize the spotlight data collected during the experiment to generate three-dimensional Fourier transforms. Unlike a stripmap mode, in a spotlight mode the SAR sensor keeps the antenna focused at one location on the ground during the entire collection. This generates a series of SAR images taken at the same location on the ocean but at different times; i.e. time series data. Stacking the images in time generates a range, azimuth, time description of the ocean surface, and a three-dimensional Fourier transform of this cube of data then generates a k_x, k_y, w description of the imagery. What was of interest to this task was to determine how the resulting (k_x, k_y, w) data differed from the known dispersion relation and whether these differences could be accounted for by existing theories. One major problem that was known *a priori* was that registration errors in the spotlight images caused by drifting of the sensor would cause a smearing in the (k_x, k_y, w) domain that would be almost impossible to remove. However, as will be discussed below, it is possible to make a measurement from the spotlight data that is insensitive to registration errors, but still sensitive to changes in the SAR MTF during the collection. These latter effects should also be a major cause of smearing in the (k_x, k_y, w) domain and can, using the measurement mentioned above, be estimated from the spotlight data.

It is important to understand how the spotlight data is generated in order to understand how it is affected by the MTF function; this is discussed in Section 4.1. Estimation of (k_x, k_y, w) data from the SAR imagery is discussed in Section 4.2, where examples of three-dimensional Fourier domain spectra are shown for two spotlight passes. Section 4.3 discusses the possible smearing effects in the (k_x, k_y, w) domain and particularly how the MTF effects can be isolated from the registration errors. Section 4.3 also discusses how a linear model for the MTF can be fit to the spotlight data to estimate the parameters of the MTF model. Finally, Section 4.4 compares the MTF

parameters estimated from the SAR spotlight data to the *in situ* measurements of the same parameters.

4.1 PROCESSING SPOTLIGHT SAR DATA

Spotlight SAR data needs to be processed differently from stripmap data due to the different manner in which it is collected. For spotlight data, every scatterer within the scene is illuminated constantly throughout the collection, whereas with stripmap data a scatterer is only illuminated when the SAR antenna beam passes over it. This implies that for spotlight data the response received by the SAR from each scatterer is slightly different, whereas for stripmap data the response is the same for any scatterer that is at the same broadside range to the sensor. Thus spotlight data must be processed with a filter that incorporates all of the different responses for each scatterer within the scene.

Figure 7 illustrates how we processed the spotlight data for this analysis. The box in the top of Figure 7 represents the scene being imaged and the first strip represents the phase history data collected by the SAR. This figure assumes that the data has been range compressed and thus consists of a collection of azimuth responses for the scatterers in the scene. Figure 7 assumes that three scatterers are in the scene, and the lines in the phase history represent the azimuth responses from each scatterer. Note that each azimuth response is shifted in the phase history due to the different azimuth location of the scatterer.

Only a piece of the phase history is processed for spotlight data; whichever piece corresponds to the time required for that image. This is illustrated in Figure 7 by the shaded region within the phase history data. Note that within the region, the azimuth response from each scatterer in the scene is different even though the scatterers are at the same broadside range. However, although they are different responses, each response is actually a shifted piece of a single response. They can therefore be Figure

SPOTLIGHT SAR PROCESSING ALGORITHM

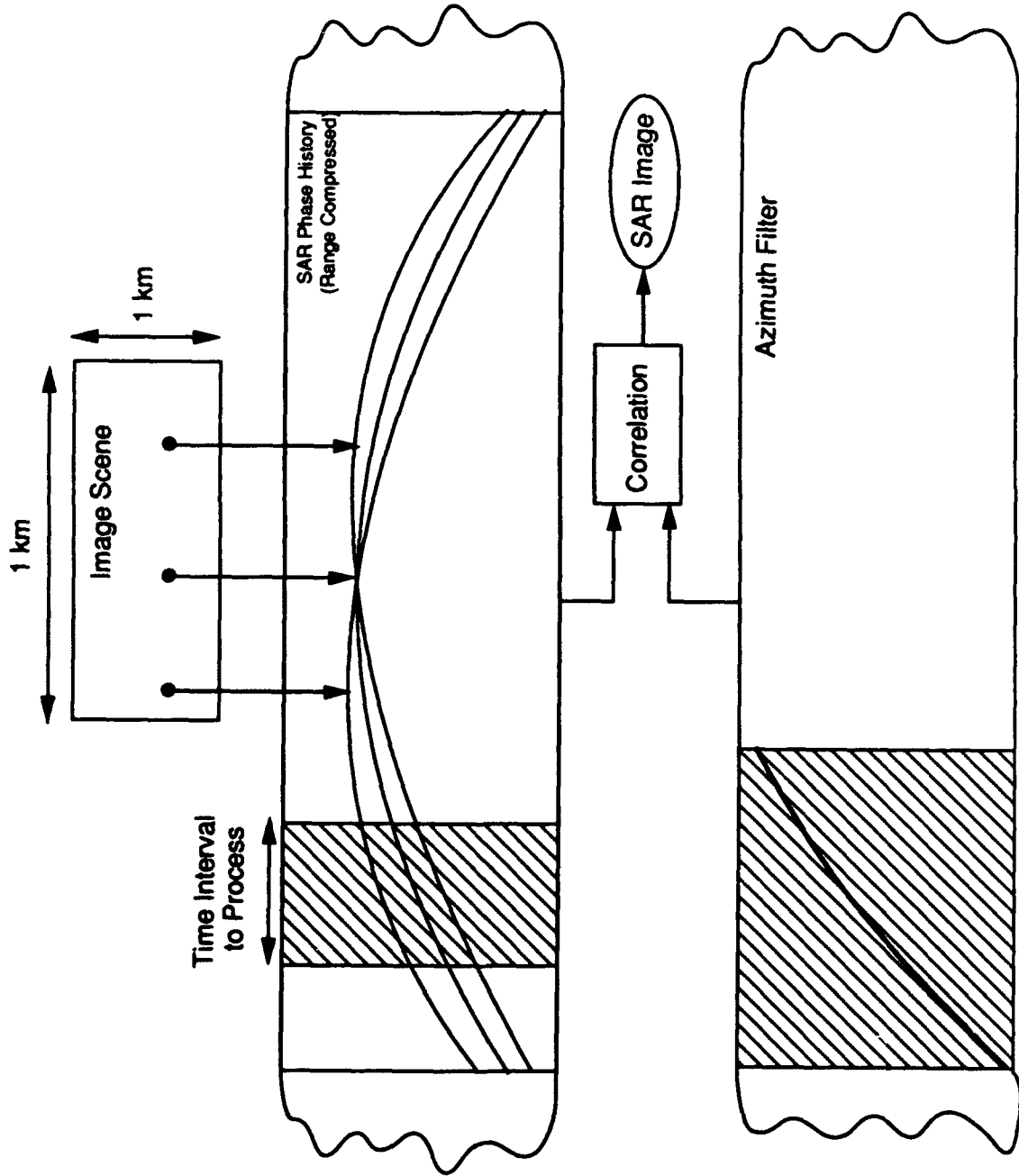


Figure 7. Schematic Illustrating How Spotlight Data Was Processed for This Analysis.

processed with a single filter, if that filter is large enough to contain the pieces of the response from each scatterer. This is illustrated in the bottom strip of Figure 7 which represents the azimuth filter. It is indicated as twice as wide as the time interval to process in the phase history data and contains only one response; however the middle portion of that response corresponds to the middle scatterer response in the shaded region of the phase history data, the left portion corresponds to the left scatterer, and the right portion corresponds to the right scatterer. Thus correlating the phase history data with the indicated azimuth filter will process all of the point targets simultaneously.

This processing algorithm has one important result for the analysis discussed below; for each spotlight image, the direction usually considered to be the azimuth direction is at a different angle. One way to define the azimuth direction is the direction along which a scatterer will be shifted if it has a radial velocity with respect to the sensor. This shift is always along the azimuth response of the scatterer. For the time interval illustrated in Figure 7, this response is rotated by some angle, so that the scatterer would not shift horizontally (i.e. in the flight direction of the sensor) but rather would shift along the indicated azimuth response at its specific angle. As the time interval to process moves closer to the middle of the scene, this azimuth direction rotates back to a horizontal position, and then rotates in the other direction as the time interval moves to the right of the middle.

The actual angle of the azimuth direction can be calculated as follows. The azimuth response follows a curve determined by the range between the sensor and the scatterer. If we let $R(x)$ be the range when the scatterer is at azimuth location x we have that

$$R(x) = \sqrt{R_o^2 + (x - x_o)^2} \quad (4)$$

where R_o is the broadside range to the scatterer and x_o is the azimuth location of the scatterer. Taking the first derivative of Eq. (4) with respect to x gives the slope of the response, the inverse tangent of which is the required azimuth rotation. Specifically

$$\theta = \tan^{-1} \left[\frac{(x-x_0)}{\sqrt{R_0^2 + (x-x_0)^2}} \right] = \tan^{-1}[\sin(\phi)] \quad (5)$$

where θ is the azimuth rotation angle and ϕ is defined as the squint angle; i.e. the angle that the sensor is from broadside. Note that Eq. (5) depends on both the range and azimuth location of the scatterer and thus is different for each scatterer. However the image scene for the P-3 spotlight mode is relatively small (1 km by 1 km) and thus the change in θ for scatterers within this scene is small and can be considered constant.

We can define the range direction for any image as pointing at the SAR, and in the slant plane this will be the squint angle defined above. Note that although Eq. (5) is approximately equal to the squint angle for small squint angles, for larger squints it can differ by a few degrees. Thus for the spotlight data the azimuth and range directions, as defined above, are not necessarily orthogonal. The difference is slight however, and we will ignore it in what follows.

Therefore, if we generate a series of SAR spotlight images using the algorithm described in Figure 7 above and register them so that the horizontal direction is along the sensor flight path, each image will have its azimuth and range axes rotated by approximately the average squint angle of the data used to generate that image. This will be most important in the MTF analysis discussed in Section 4.3.

4.2 GENERATING THREE-DIMENSIONAL FOURIER TRANSFORMS

There are two main algorithms for generating three-dimensional spectra from spotlight data. The first is the most conceptually straightforward -- stack the images in time to generate a cube of digital samples and then perform a three-dimensional Fourier transform on the cube. The second algorithm involves utilizing the ambiguity function [3] of the range compressed phase history data. Both algorithms were analyzed and it was determined that the spectral estimates they provided were essentially equivalent, however the ambiguity algorithm approach suffered from more

complicated implementational difficulties. Thus for this analysis we choose the simply, time stacking approach. A paper describing the mathematics used to analyze the two approaches as well as a more detailed description of the ambiguity function algorithm was published in the IGARSS '92 proceedings and is included as the Appendix.

Figure 8 illustrates the time stacking approach that was used. Due to the way that a SAR collects data in the spotlight mode, each SAR image is of the same location on the ocean surface but is taken over a different time interval. If the integration time for each image is small compared to the period of the dominant wave, we can consider each SAR image to be a snapshot of the ocean surface at a constant time; say the middle time of the integration period. Thus the spotlight SAR imagery represents a cube of data as shown in the left illustration in Figure 8; each spotlight image contains samples that vary over the along track and cross track directions but which were collected at a constant time. If we perform a three-dimensional Fourier transform on this data, we will get the three-dimensional spectrum in coordinates k_x , along track spatial frequency, k_y , cross track spatial frequency, and w , temporal frequency. This is illustrated in the right diagram of Figure 8. Implementationally this is done by first performing two-dimensional Fourier transforms on each spotlight image, and then performing one-dimensional Fourier transforms for each "column" in Figure 8. That is, for a constant (k_x, k_y) location in each 2-D spectrum of the SAR imagery one considers the complex-valued data from each spectra to represent samples of a function in time, and a one-dimensional Fourier transform of this data then generates a plot through w values at that (k_x, k_y) location. Performing such a one-dimensional Fourier transform on every (k_x, k_y) sample in the image spectra generates the final 3-D spectrum.

To make the 3-D spectral estimate more accurate there are some known SAR imaging effects that should be removed. The most dominant is the SAR antenna pattern weighting which introduces a modulation in both range and azimuth for each SAR

CES-92-083a

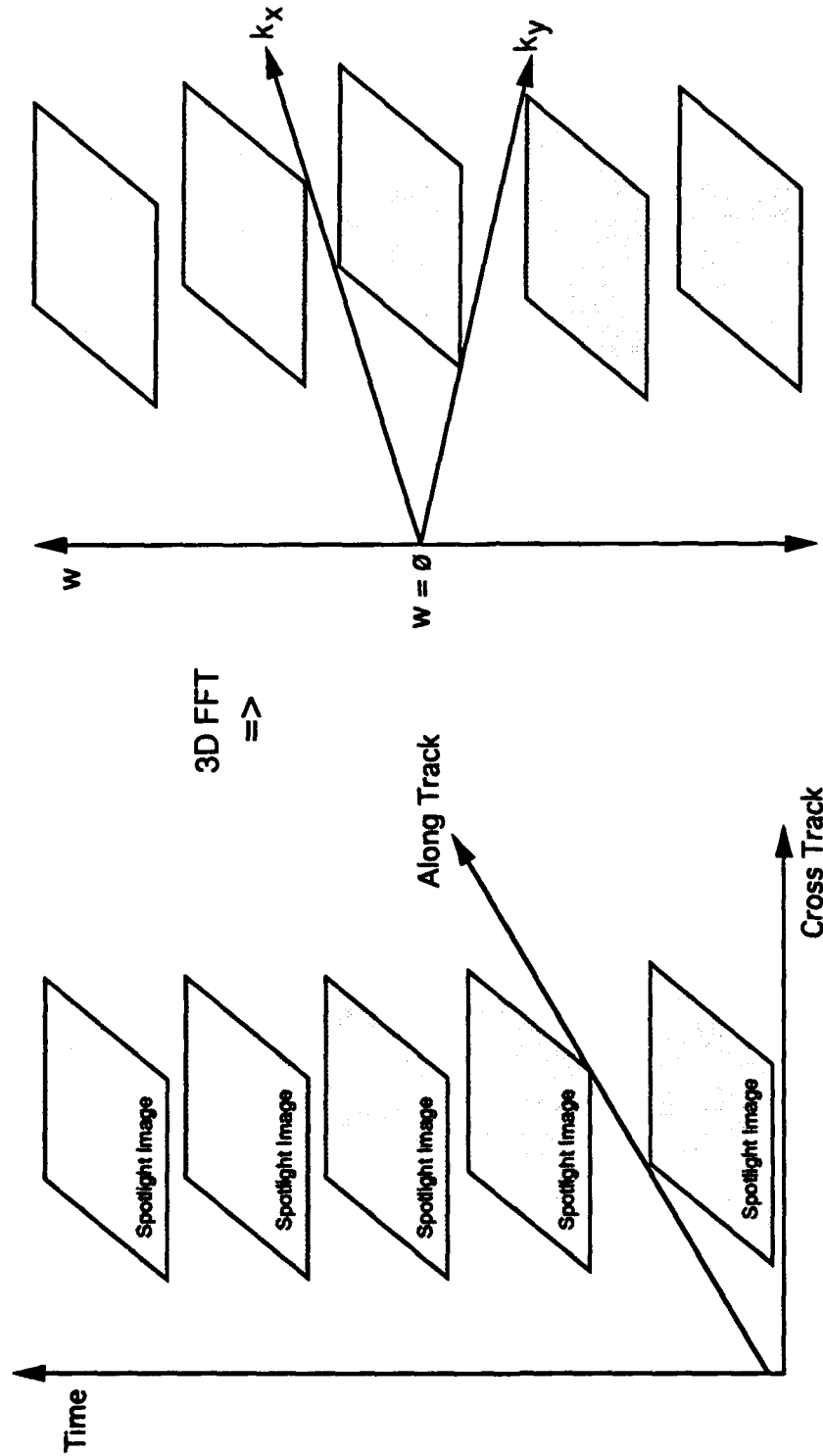


Figure 8. Schematic Illustrating How Three-Dimensional Fourier Transforms are Generated From Spotlight Imagery.

spotlight image. In addition, since each image is registered to be in along track and cross track coordinates, the antenna pattern will be rotated at a different angle in each image; approximately equivalent to the squint angle for that image. If not removed, this changing modulation will introduce significant smearing in the final 3-D spectrum. Our method of removal is to smooth each image with a large median filter so that only the low frequency modulations in the image survive the filtering. This highly smoothed image estimates the two-dimensional antenna pattern and the original SAR image is divided by it. We normalize the antenna pattern estimate to have unit mean before performing the division in order to not change the scale of the SAR imagery.

A second effect is the IPR of each SAR image. This essentially represents the limited resolution of the imagery and manifests itself as a weighting on the two-dimensional spectra formed from each image. Because of the rotation of range and azimuth coordinates for each image discussed above, this IPR spectral weights also rotates for each spectrum causing, for a given (k_x, k_y) location, a modulation of the spectra in time and thus a smearing in the w direction. It can be removed using the algorithm described in Section 2.0 that generated the corrected spectra, however we have found that it is a small effect for the data analyzed below and that removing it had no affect on the results.

A third effect is the SAR MTF which relates ocean surface waveheight data to SAR imagery spectra. In a linearized version this manifests itself as an additional weighting on the spectra of the individual SAR images which also rotates for each image. This is a much more significant effect than the IPR weighting and will be discussed in more detail below.

Finally there is a major effect caused by registration errors in the SAR sensor. The discussion so far has implicitly assumed that the SAR images are of the same location on the ocean surface. This will not be true if the SAR sensor is wandering from its desired track. Such wandering introduces a shift into each image relative to its

consecutive images which manifests itself as a phase error in the SAR image spectra. When the final one-dimensional Fourier transforms are done on the image spectra, this phase function will cause a smearing along the w axis. This is the one dominant error that we had no control over. We attempted to register the images using the tower response if it was in the scene, but this proved to have too extended of a signal and thus not be highly correlated from image to image. We will see below that we can still make estimates of the SAR MTF using the intensity of the two-dimensional image Fourier transforms (which will be insensitive to registration errors since these only effect the phase of the image Fourier transforms) but that smearing along the w axis most probably caused by these registration errors will still be in the data.

Figure 9 is a flowchart which summaries the full algorithm we used to generate our spectral estimates with all the possible corrections indicated (except for a correction for registration errors). Figure 9 also shows a correction for a speckle bias in the two-dimensional image spectra which we did not perform since it does not cause any smearing in the final three-dimensional spectrum. As indicated in Figure 9 by the dashed line, we usually went right from the two-dimensional image Fourier transforms to the final one-dimensional time Fourier transform without performing the IPR (or speckle bias) correction or the MTF correction. As mentioned above the IPR correction was insignificant. For the MTF analysis we never corrected the whole image spectrum but only the portion corresponding to the dominant wave spectrum; this is discussed below in more detail.

Using the algorithm shown in Figure 9 (without the IPR and MTF corrections) we generated three-dimensional spectra for the three spotlight data passes during Nov. 6; passes 8, 14 and 28 which represented a low altitude (5000 feet) medium altitude (10000 feet) and high altitude (20000 feet) case, respectively. The early analysis concentrated on the first two passes (8 and 14) since the higher altitude pass represented more significant MTF effects. The middle and higher altitude passes however were

3-D SPECTRUM ESTIMATION APPROACH

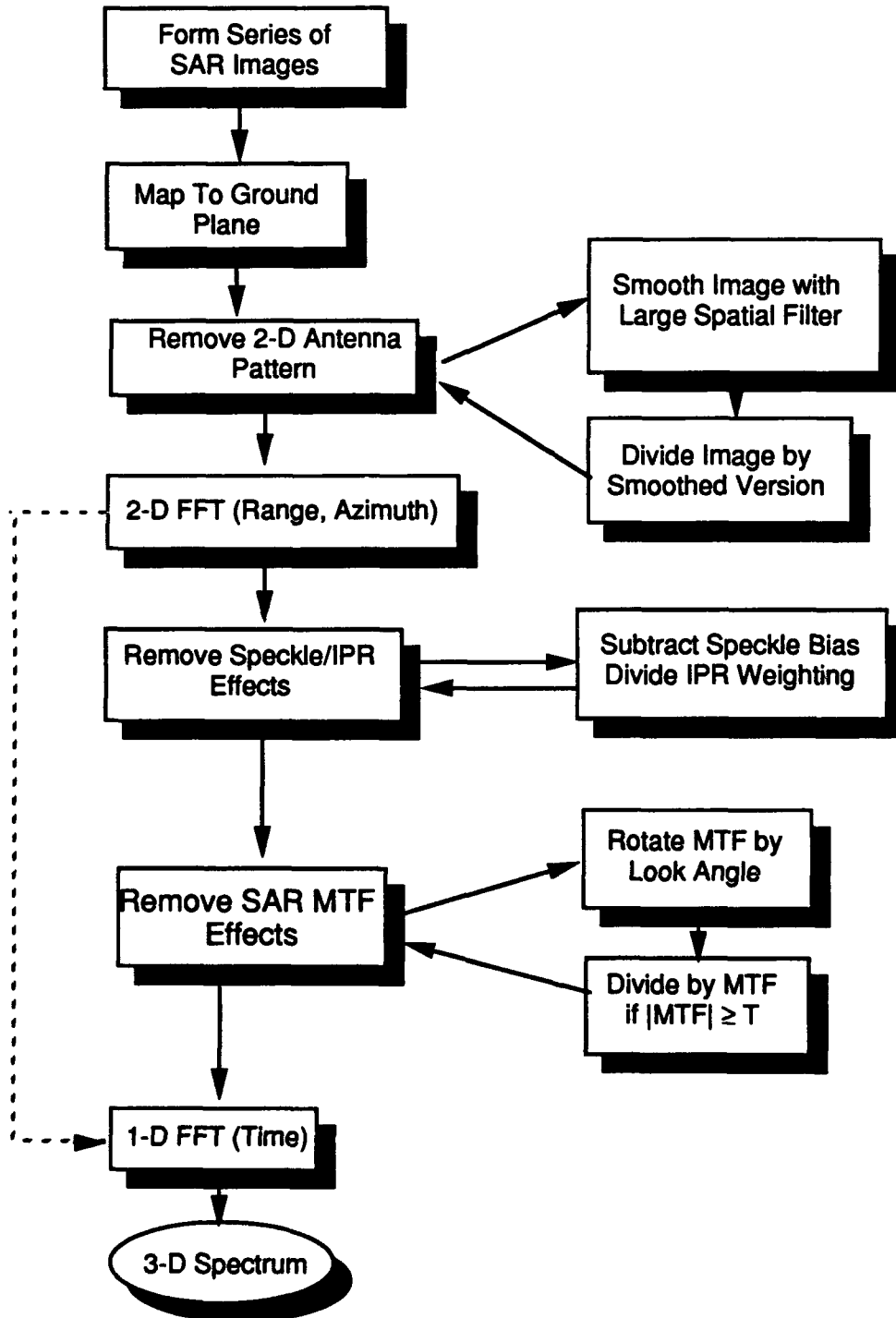


Figure 9. Flowchart Showing the Algorithm, With Corrections, for Generating Three-Dimensional Fourier Transform Data.

used for the MTF analysis discussed below. For each case 32 spotlight images were generated using a 1.5 second integration time and separated by 1.5 seconds. The dominant wave for Nov. 6 was approximately a 90 meter wave travelling in the cross track direction. The period for such a wave is approximately 7.5 seconds and thus the integration time is a small fraction of the dominant wave period. Figure 10 shows an example of the spotlight imagery from pass 8. Every other image is shown, resulting in 16 images. The horizontal direction is the cross track direction and the vertical is the along track. The left edge of each image is the near range and the right edge is the far range. There are approximately seven wavelengths of the dominant wave across each image and they are propagating from the far range (right) to the near range (left). The images increase in time from the upper left to the lower right and sequentially along each row from left to right. Note an apparent rotation effect from the early time images (upper left) to the later time (lower right). This is caused by the SAR IPR weighting producing a smearing in the azimuth direction, however the azimuth direction is rotating as a function of time as discussed above.

Figure 11 shows the spectra from each of the images in Figure 10. Again this is every other image so only 16 are displayed. The spectra in Figure 11 have been highly saturated so that the wave peaks are invisible. What can be seen are the two dominant spectra weightings discussed above; the IPR and MTF weightings. The small cigar shaped rotating about the middle of the spectra represents the MTF weighting. It is dominated by the azimuth falloff term (see Section 4.3) which is rotating with the azimuth direction. The slightly dimmer cloud around this is the IPR weighting. Note that it also rotates with the azimuth direction in each image, but in addition it changes shape significantly. However, as mentioned above, we found that this weighting did not have a significant impact on the analysis and thus we ignored it.

Saxon FPN Spotlight SAR Image Data
Nov. 6 Pass 8
Look Angles -27 to 30 degrees

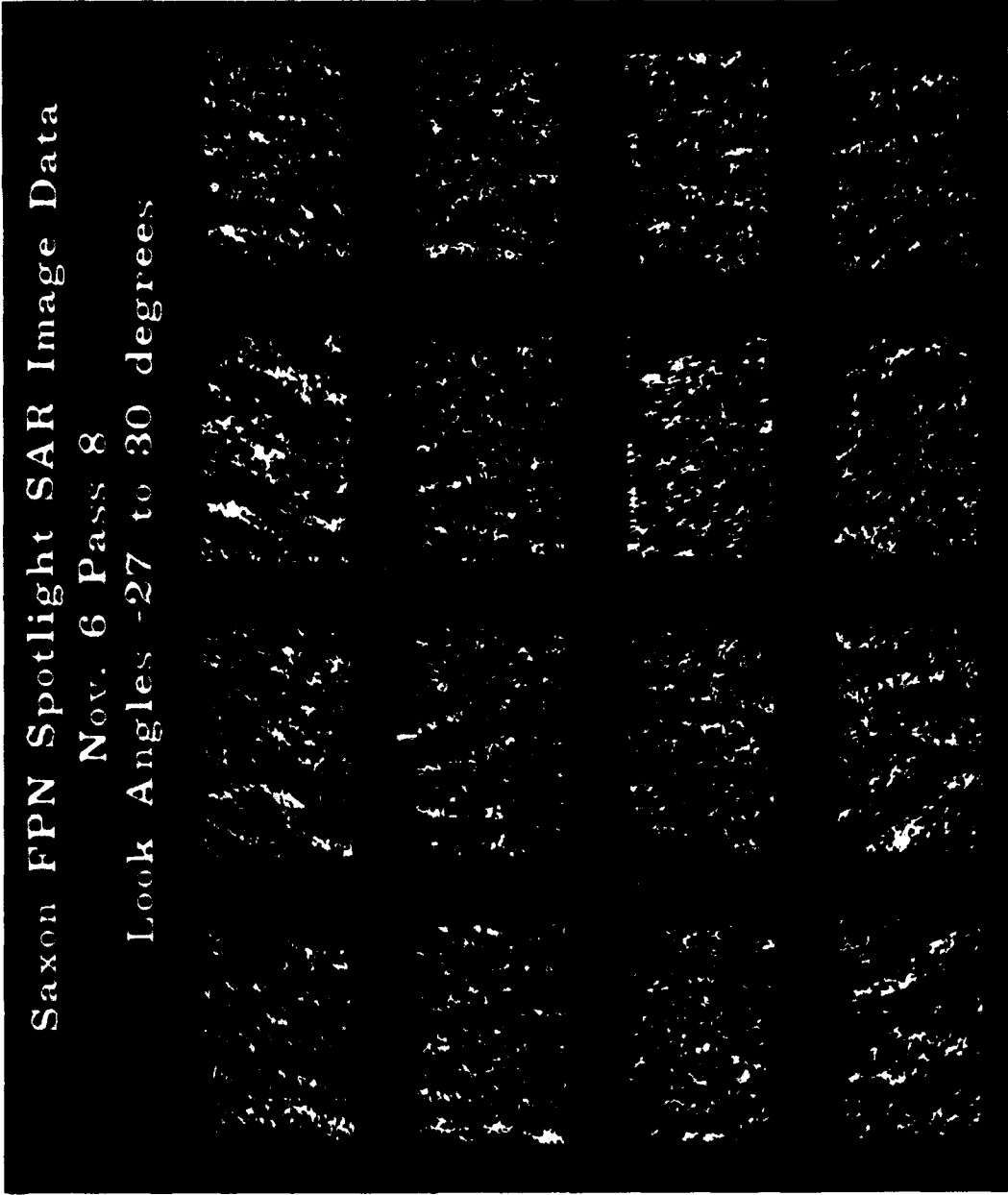
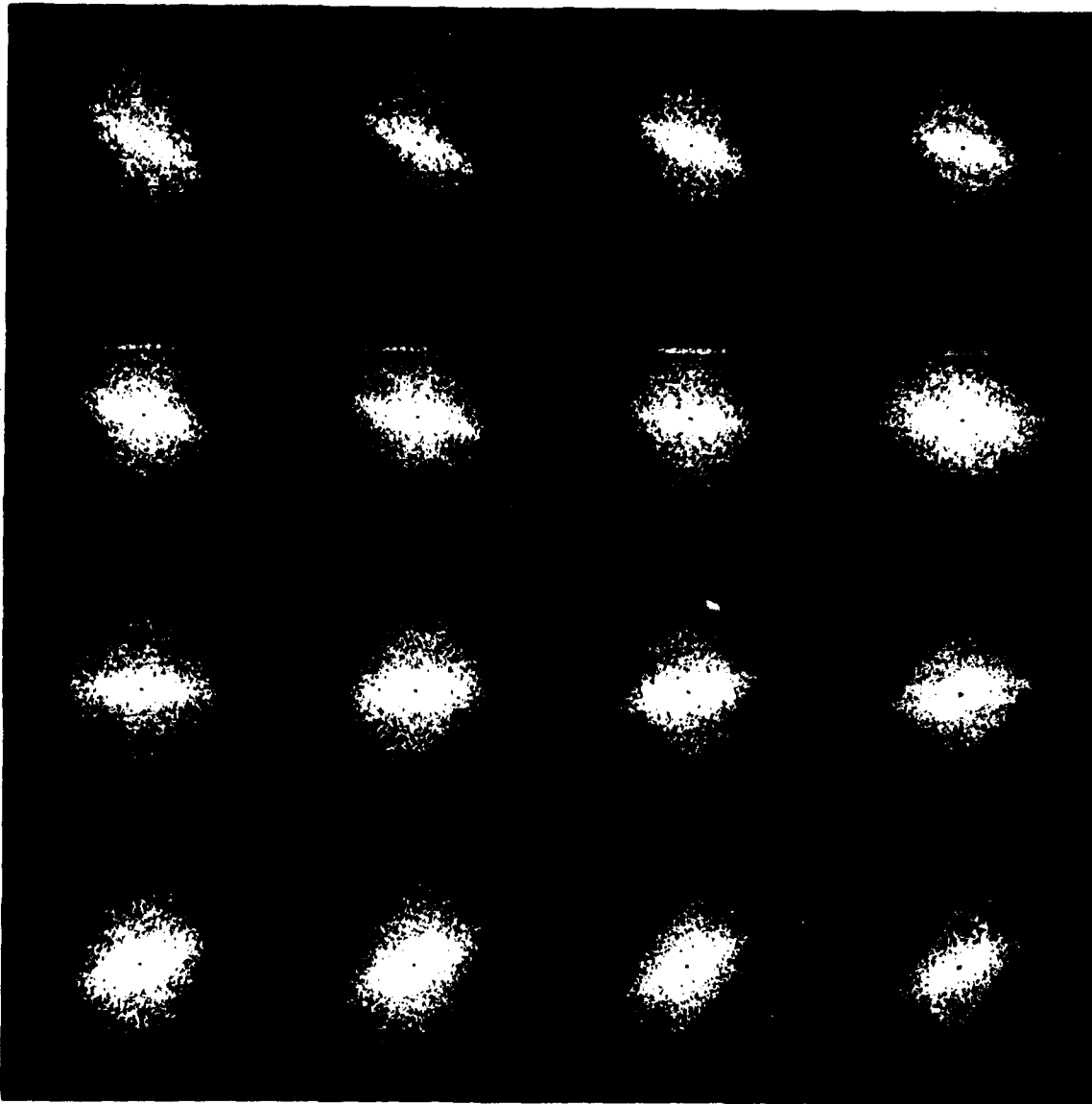


Figure 10. Example of Spotlight Imagery From Nov. 6 Pass8. Every Other Image is Shown.

92-10899-3



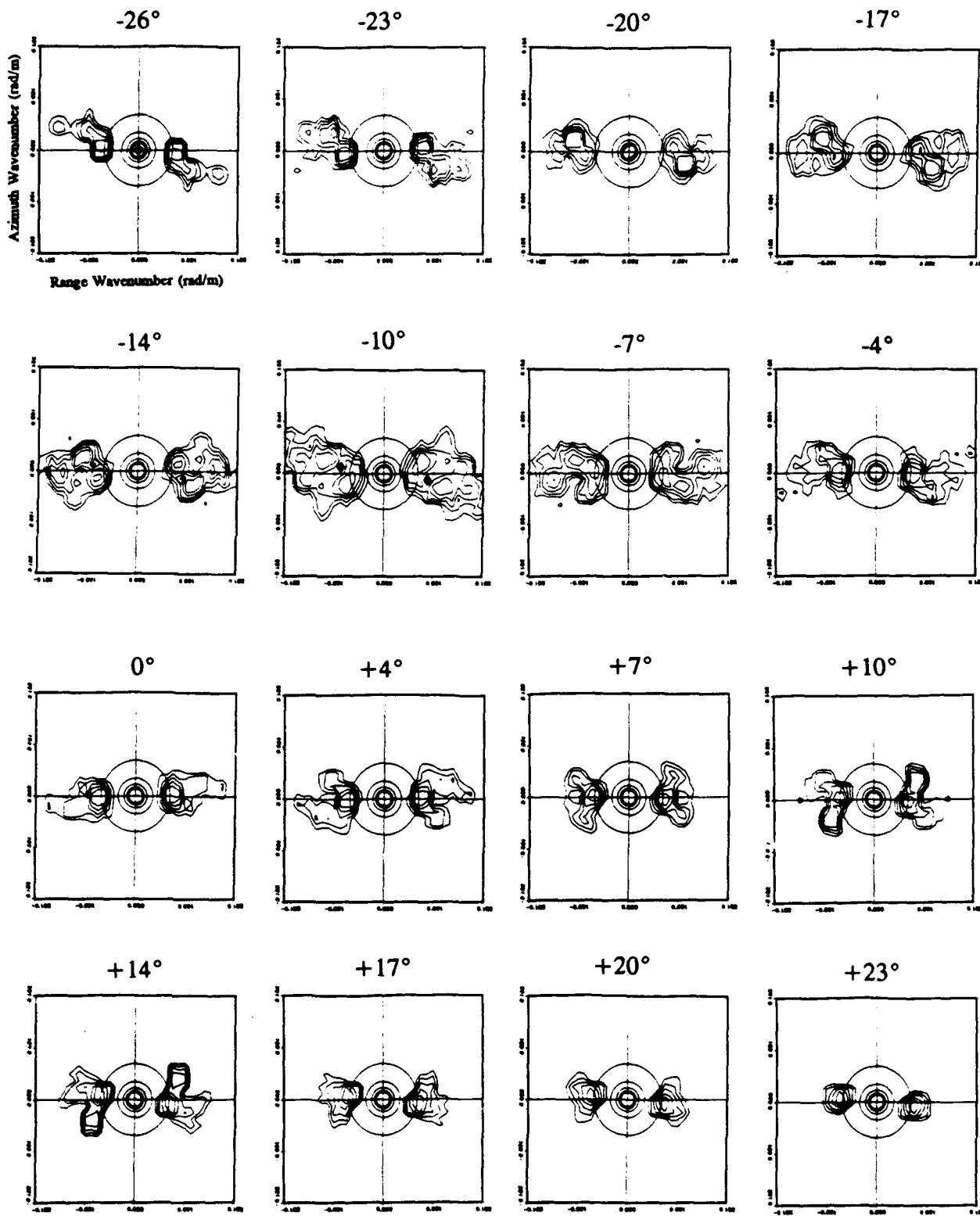
**SAXON-FPN SPOTLIGHT DATA
NOV. 6 PASS 8
LOOK ANGLES -26° to $+23^{\circ}$
SATURATED SPECTRA**

Figure 11. Example of Image Spectra From Nov. 6 Pass 8. Spectra are Highly Saturated to Illustrate the MTF and IPR Spectral Weightings. Every Other Spectra is Shown.

92-10539

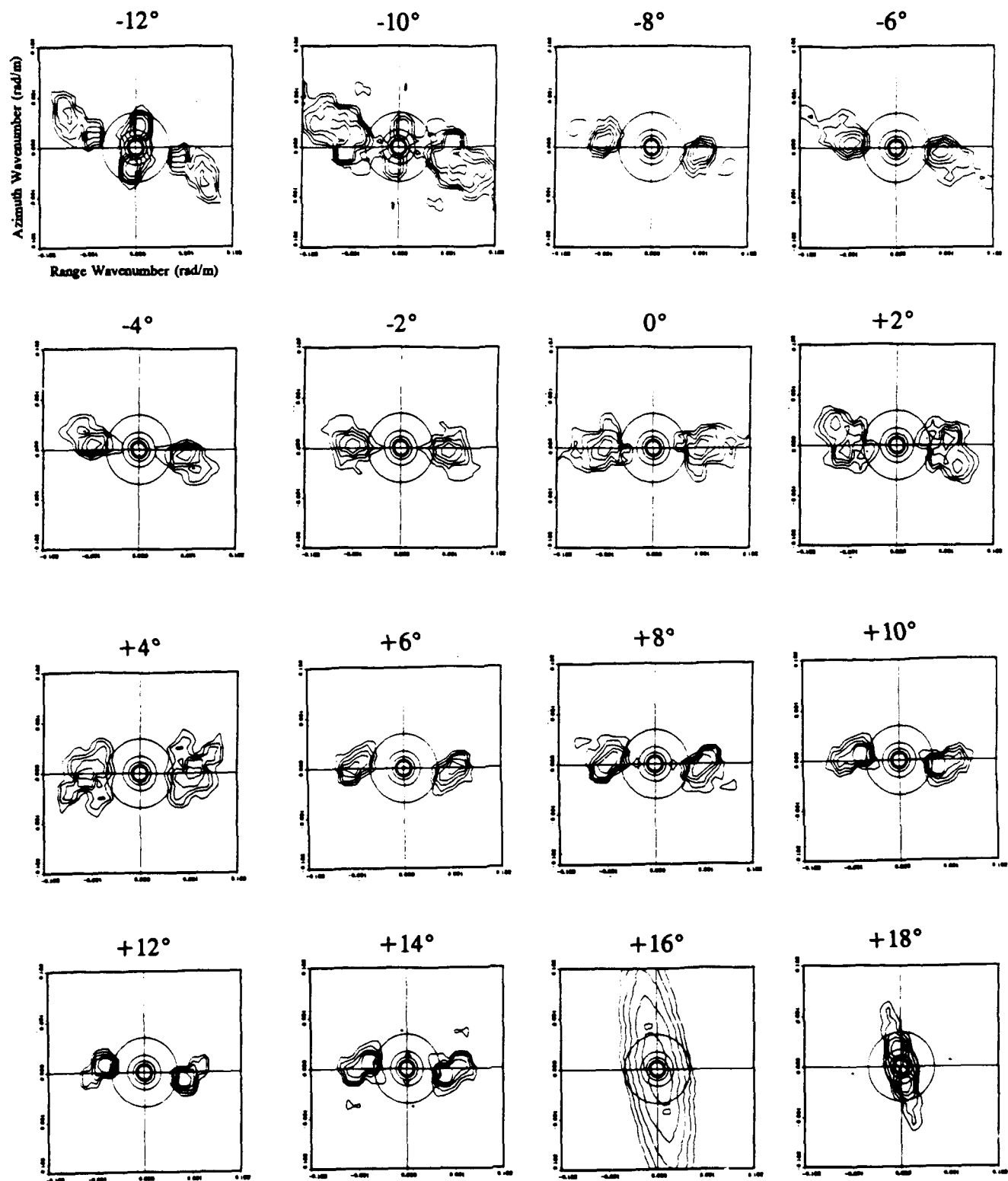
Figures 12 and 13 illustrated what the dominant wave peaks are doing in each spectra (as opposed to what the spectra weightings are doing as was illustrated in Figure 11) for passes 8 and 14. These are contour plots of the dominant wave peaks as a function of time (and therefore squint angle). The squint angle for each spectra is indicated at the top and the largest circle in each plot represents a 100 meter wave. The contours are every 1 dB. It is interesting to note that there is not a significant change in the location of the dominant wave peaks for either pass; although pass 14 does show a hint of a splitting in the spectrum at a squint angle of +2 degrees. To quantify this we located the position of the peak in each spectra. These dominant wavelengths and wave directions are plotted in Figures 14 and 15 as a function of look angle (which is equivalent to squint angle defined above). The lower altitude pass shows more variability than the middle altitude pass, although both show angle variations that are less than ± 14 degrees. The dotted line on each wave angle plot is the expected dominant wave angle if the SAR was only picking out the range component of the wave; i.e. the dominant wave angle would be equal to the SAR look angle. Note, however, that throughout pass 14 and in the early part (negative look angle) of pass 8 the dominant wave number is shorter than 90 meters, sometimes as low as 60 meters. The spectral resolution of the data was such that the dominant wave length could range from 75 to 105 meters, but not as low as 60 meters. This was a discrepancy we were not able to resolve.

Because it is sometimes of interest to the theories, we also plotted the average spectral intensity and maximum spectral intensity for each pass. These are shown in Figure 16 and 17. For pass 14 there appears to be large noise effects at the edges of the collection and these should be ignored. For both passes the peak spectral values appear to be around 0 degrees look angle which would represent the look direction being into the propagation direction of the waves.



SAXON-FPN Spotlight Data Nov 6 Pass 8

Figure 12. Contour Plots of Dominant Wave Peaks in Spotlight Spectra From Nov. 6 Pass 8. Every Other Spectra is Shown.



SAXON-FPN Spotlight Data Nov 6 Pass 14

Figure 13. Contour Plots of Dominant Wave Peaks in Spotlight Spectra From Nov. 6 pass 14. Every Other Spectra is Shown.

SAXON-FPN SPOTLIGHT DATA NOV 6 PASS 8

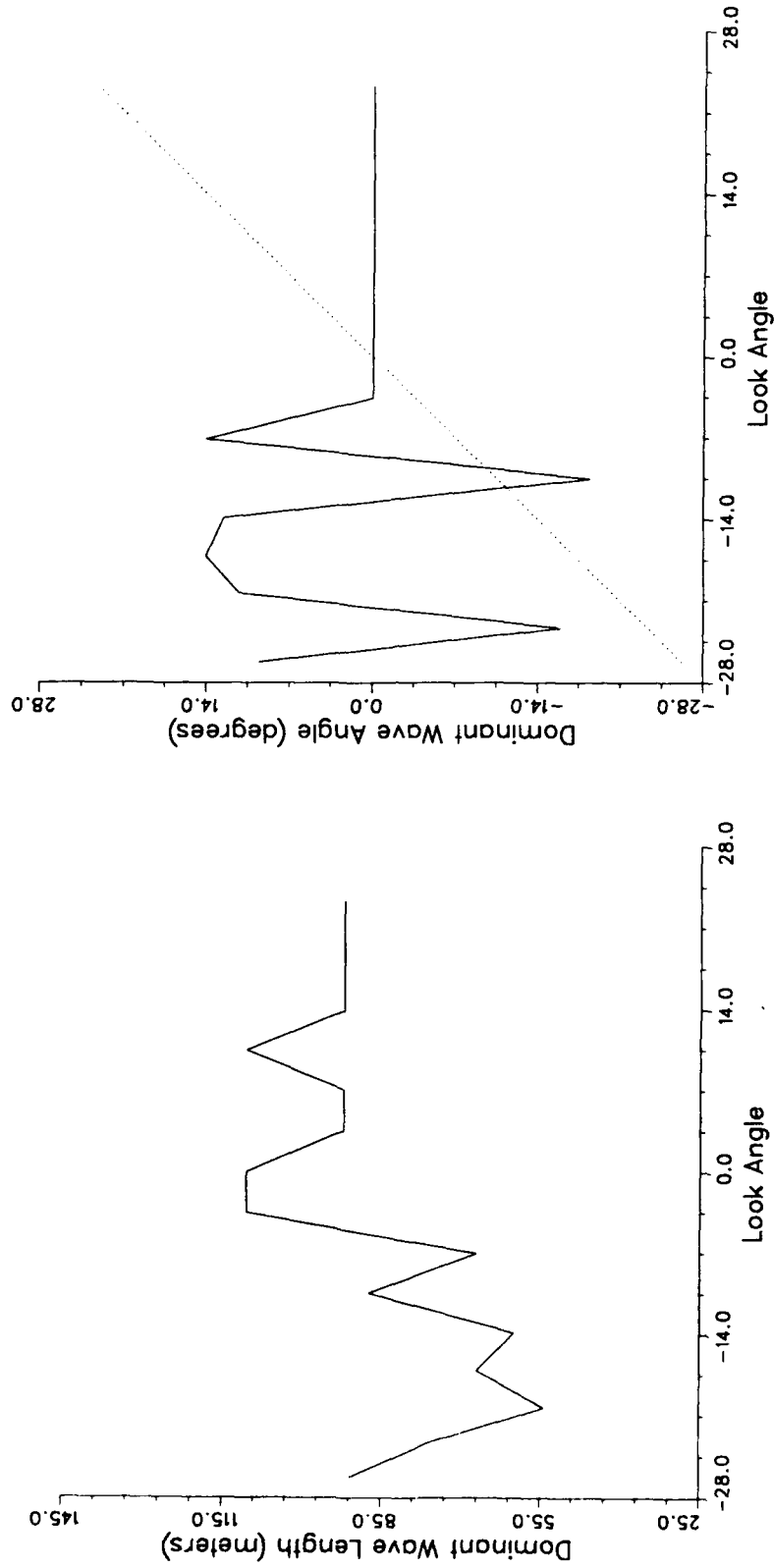


Figure 14. Dominant Wave Length and Wave Direction Versus Look Angle (i.e. Squint Angle) for Nov. 6 Pass 8 Spotlight Data.

SAXON-FPN SPOTLIGHT DATA NOV 6 PASS 14

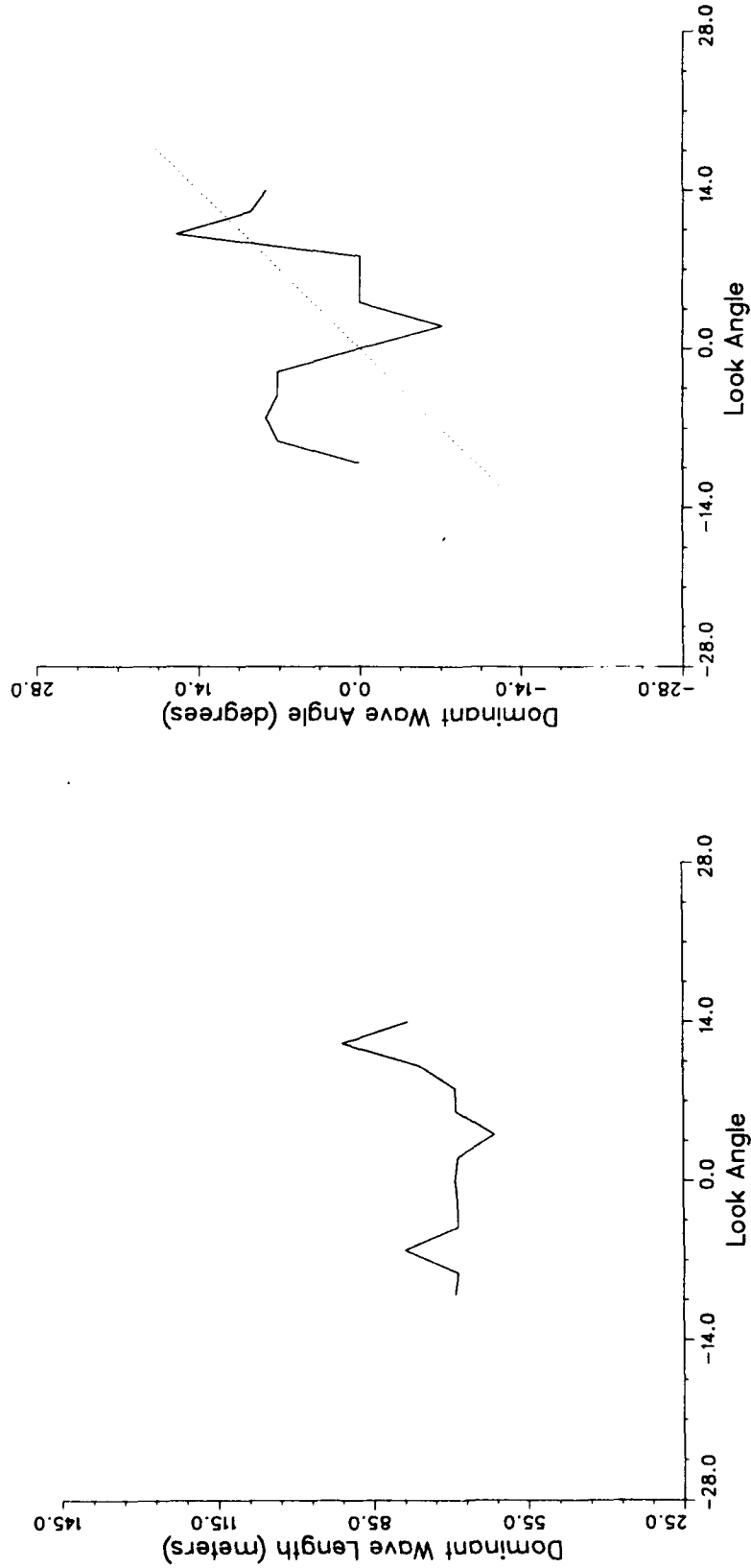


Figure 15. Dominant Wave Length and Wave Direction Versus Look Angle (i.e. Squint Angle) for Nov. 6 Pass 14 Spotlight Data.

SAXON-FPN SPOTLIGHT DATA NOV 6 PASS 8

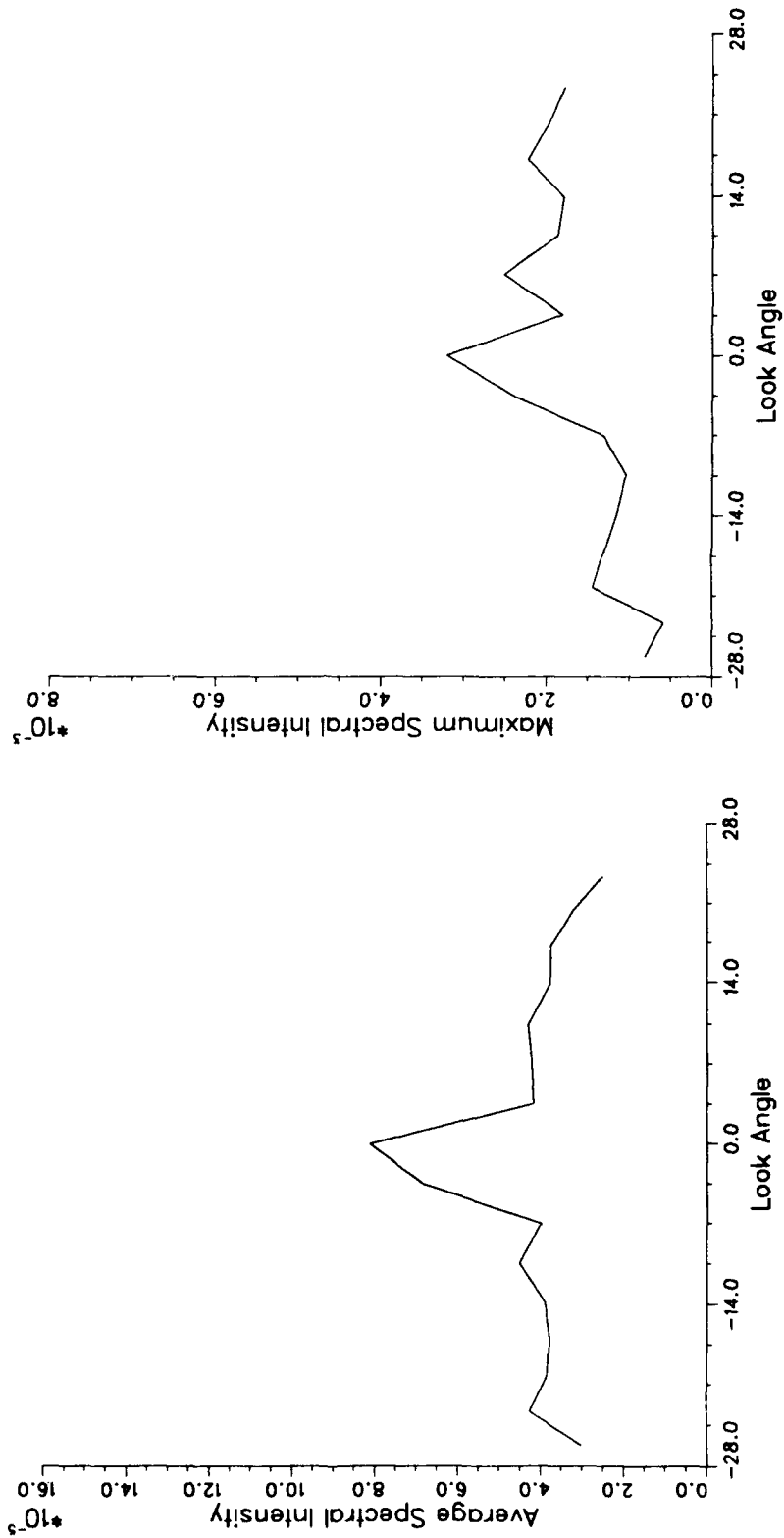


Figure 16. Average Spectral Intensity and Maximum Spectral Intensity for Nov. 6 Pass 8 Spotlight Data.

SAXON-FPN SPOTLIGHT DATA NOV 6 PASS 14

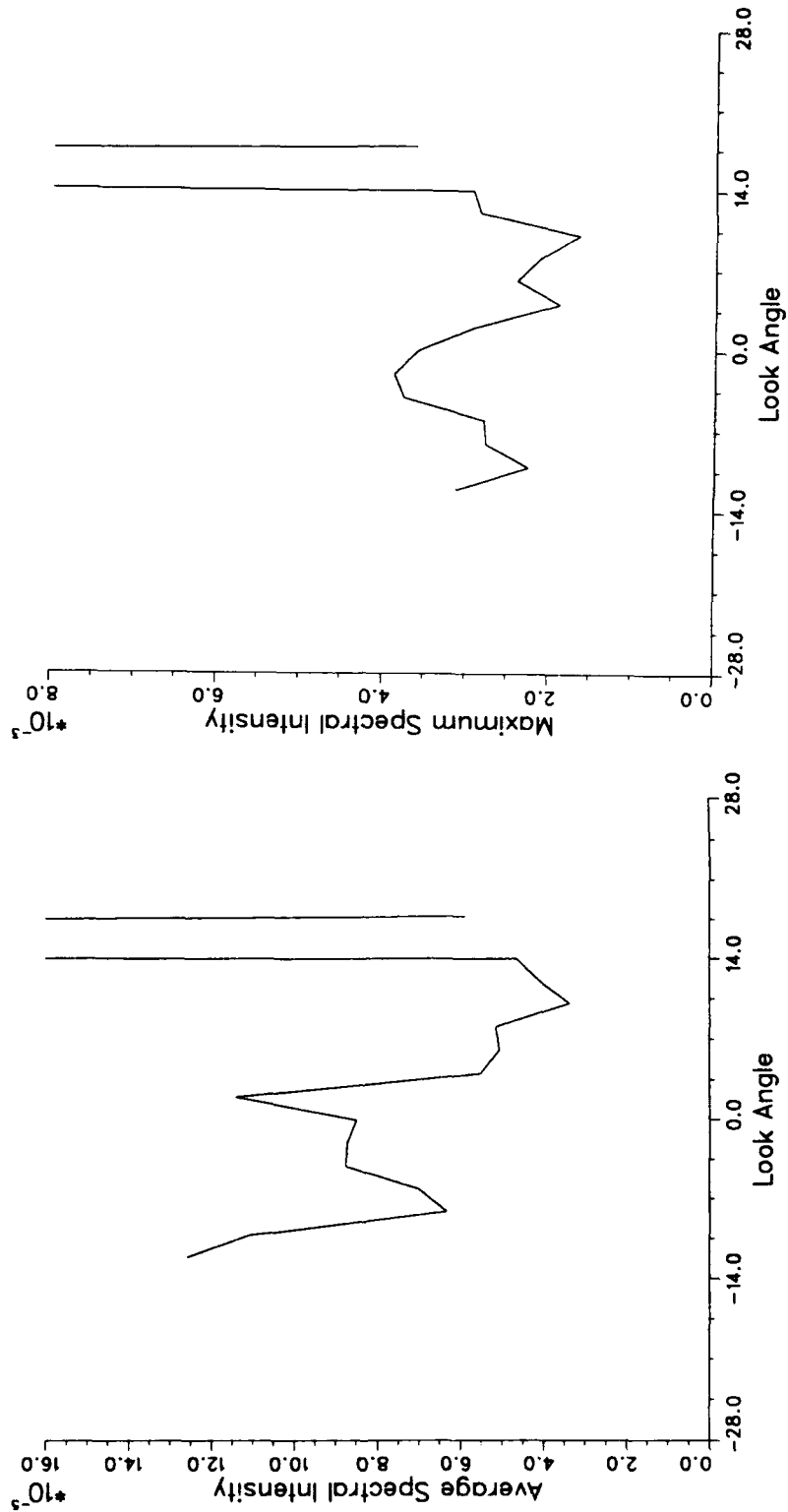
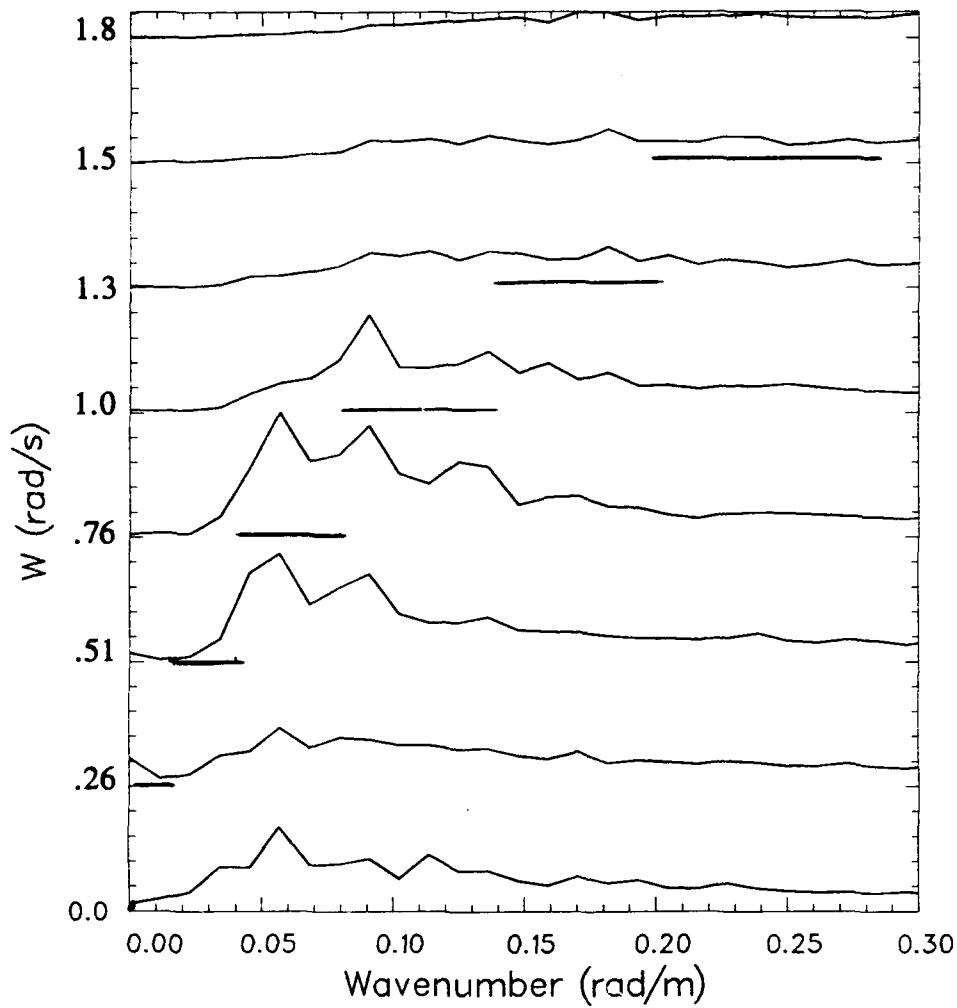


Figure 17. Average Spectral Intensity and Maximum Spectral Intensity for Nov. 6 Pass 14 Spotlight Data.

Finally, we performed the final one-dimensional Fourier transform of the spectra to generate the (k_x, k_y, w) data. For a given w value we integrated the (k_x, k_y) plane over angles to generate a one-dimensional plot versus wavenumber, $k = \sqrt{k_x^2 + k_y^2}$. A cascade plot of these curves for each w value is shown in Figure 18 for pass 8. For this pass we were able to remove most of the registration error by using the response of the SAXON-FPN tower in each image to shift the images relative to each other. However, due to the extended and changing nature of the tower response, this still left some residual errors. The bars drawn beneath each curve represents the range of wavenumbers, $k = w^2/g$, that correspond to the dispersion relation for the w value. There is a range of values due to our sample spacing along the w axis. The dominant wave should lie on an w value of 0.83 and a wavenumber of 0.07. This is relatively consistent with the data; the $w = 0.76$ curve (the closest to the actual w value) shows the dominant energy and it peaks at approximately the right location for the dispersion relation. There is a fair amount of smearing in the data however; we are not seeing delta-like functions following the dispersion curve but rather very elongated functions. Figure 19 shows the full (k_x, k_y) planes for 16 different w values; these are the lower 16 w planes where the dominant wave energy should be located based on its propagation direction. The w values increase from the upper left to the lower right in Figure 19. The green samples indicate the spectral energy in each plane. The red dot in each plane represents the (k_x, k_y) location for that plane that corresponds to the dispersion relation for waves traveling in the cross track (horizontal) direction. The dominant wave energy should be located between the seventh and eighth w planes in Figure 19 and note that these planes do contain the brightest spectral values and are consistent with the dispersion relation (i.e. the red dot is within the spectral energy). However it can be seen from Figure 19 that the energy in these w planes is being smeared to the consecutive planes in the same (k_x, k_y) locations making these outer



**3-D Spectrum From SAXON-FPN Spotlight Data
Nov 6 Pass 8**

Bars Indicate Dispersion Curve

Figure 18. Three-Dimensional Fourier Transform of Nov. 6 Pass 8 Spotlight Data Collapsed into a Series of w vs. k Plots. Bars Indicate Ranges of k Values for a Given w Sample.

SAXON-FPN Nov 6. Pass 8
3D SAR Spectrum
w Range 0 to 2.0

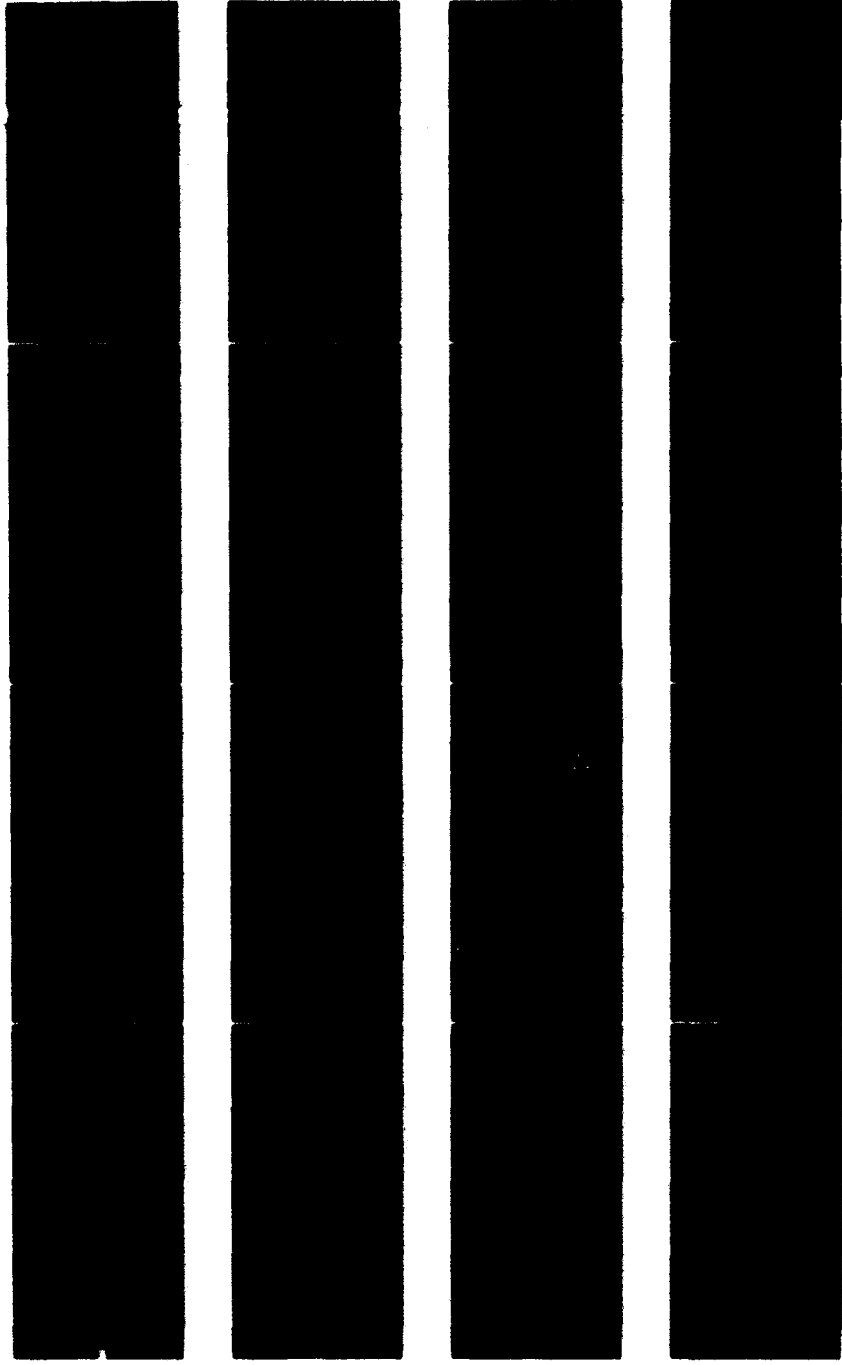


Figure 19. Three-Dimensional Fourier Transform of Nov. 6 Pass 8. Spotlight Data Shows 16 w Planes. Green Values Indicate Spectral Energy, Red Dot Indicates Dispersion Relation for Range Traveling Waves.

92-11583

planes inconsistent with the dispersion relation. One can see from this expanded view in Figure 19 that this is one of the major causes of smearing in Figure 18.

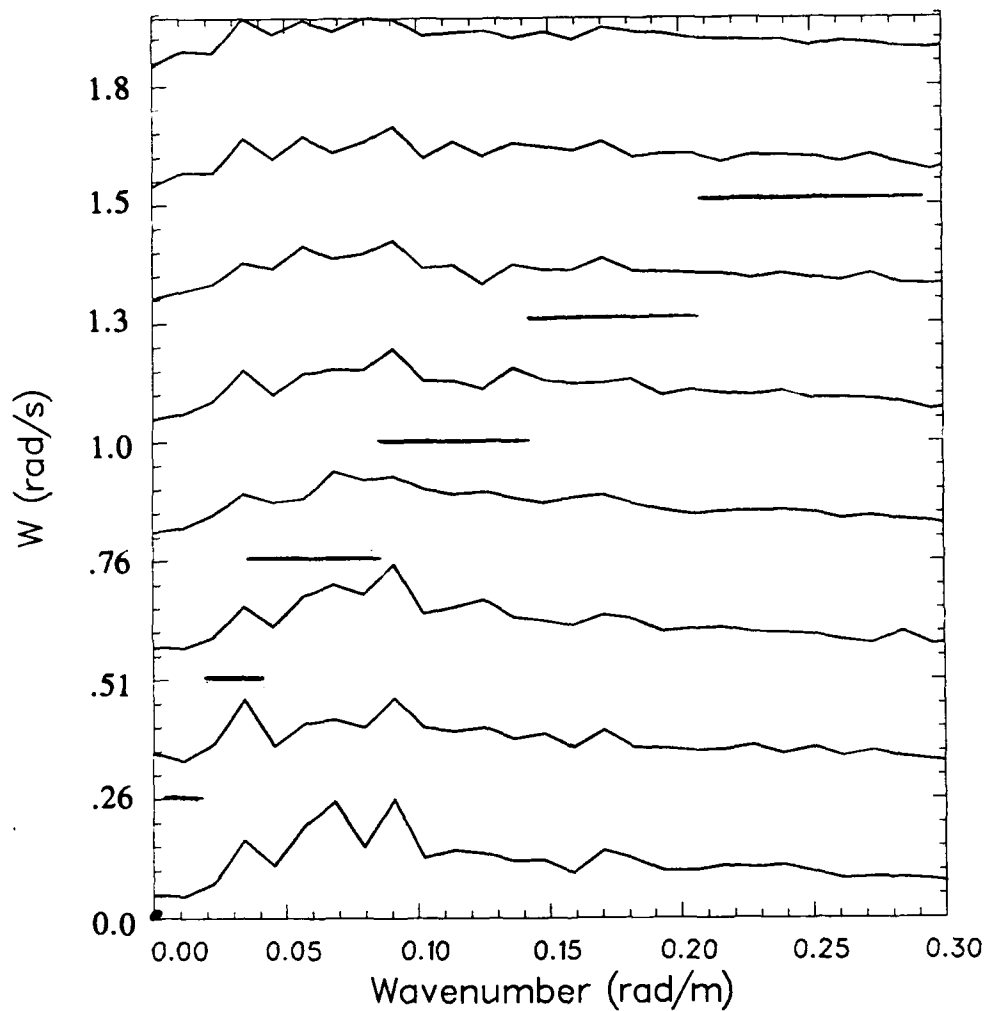
Thus for pass 8 we were able to demonstrate that a three-dimensional Fourier transform of the spotlight data did in fact peak at locations in (k_x, k_y, w) that were consistent with the dominant wavenumber and direction, and consistent with the dispersion relation. However there was also a large amount of smearing in the (k_x, k_y, w) domain resulting from the causes discussed above. Below we will discuss how we utilized this smearing to estimate parameters for the SAR MTF.

We also attempted to do this analysis on the middle altitude data from pass 14. However the results were inconclusive, most probably due to the fact that we could not remove any of the registration errors for this pass since the tower was not included in the images. Figure 20 shows a similar plot to Figure 18, but this data seems inconsistent with the dispersion relation and no clear peak is visible. We did not form the expanded images for this case due to these inconclusive results.

4.3 ESTIMATING MTF PARAMETERS FROM THE SPOTLIGHT DATA

In the previous section we saw that for Nov. 6 pass 8 a three-dimensional Fourier transform of the spotlight data generated spectral values that were consistent with the dispersion relation but that had a fair amount of smearing in the spectral domain. In this section we will investigate this smearing in a little more detail, and show that there exists a measurement (intensities of the SAR image Fourier transforms as a function of time) which is dominated by one of the major causes of smearing, the SAR MTF, and unaffected by the other, registration errors. We will attempt to use this measurement to estimate parameter values for the MTF.

Figure 21 illustrates a method of understanding the smearing in the (k_x, k_y, w) domain that will be useful to what follows. The top illustrations show the first step in generating the three-dimensional transforms; two-dimensional Fourier transforms are



**3-D Spectrum From SAXON-FPN Spotlight Data
Nov 6 Pass 14**

Bars Indicate Dispersion Curve

Figure 20. Three-Dimensional Fourier Transform of Nov. 6 Pass 14 Spotlight Data Collapsed Into a Series of w vs. k Plots. Bars Indicate Range of k Values for a Given w Sample.

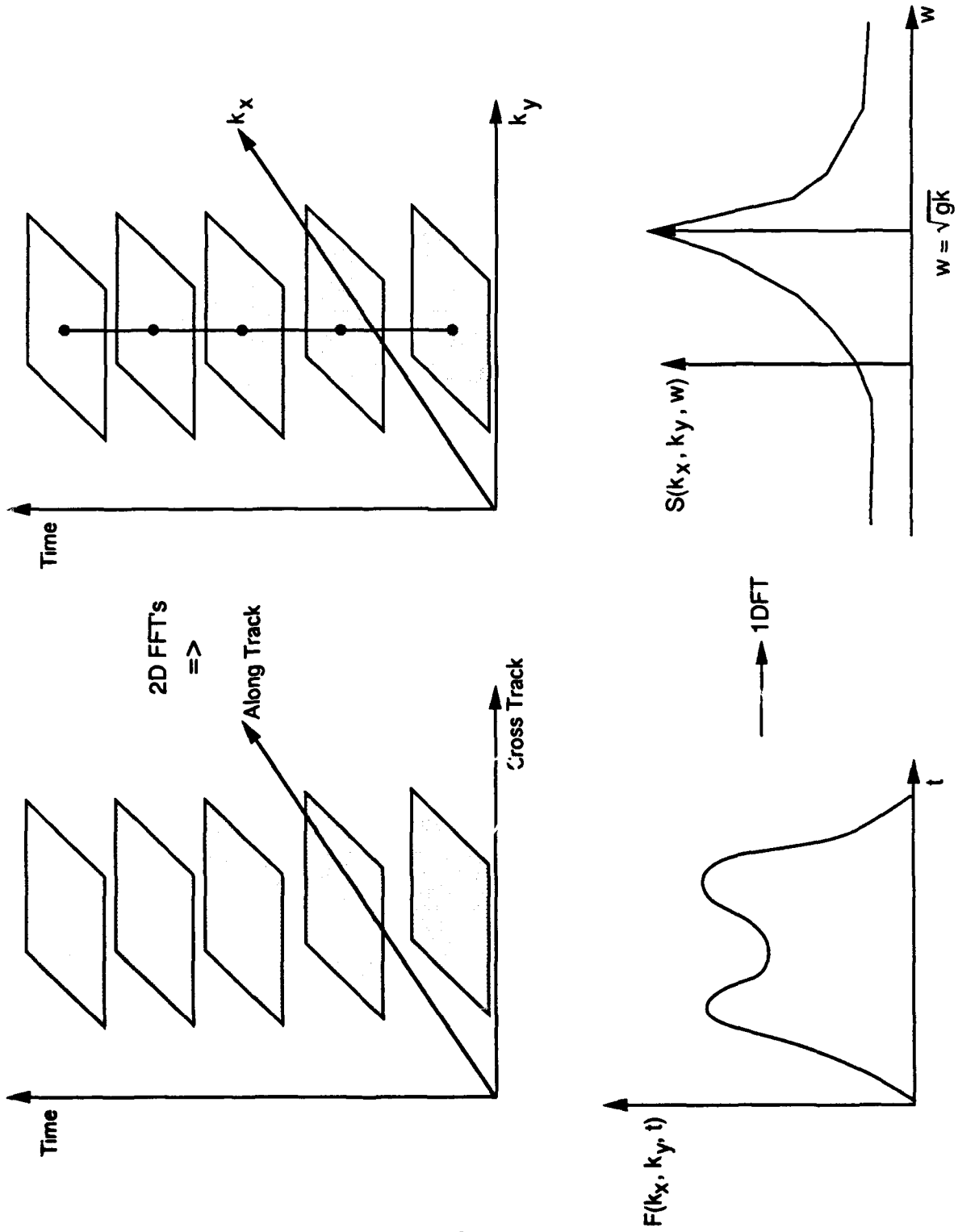


Figure 21. Schematic Illustrating How Weighting on Image Spectra Versus Time Causes Smearing in Three-Dimensional Fourier Data.

performed on the image data stacked in time to generate spectral data $F(k_x, k_y)$ at different times. For a given (k_x, k_y) location we could plot the spectral data as a function of time along the line indicated in Figure 21, which would result in a function of time as shown in the bottom left plot. A one-dimensional Fourier transform of this function would then generate a function of w ; in fact this would be a cut through the three-dimensional spectrum, $S(k_x, k_y, w)$ at the specific (k_x, k_y) location. Ideally this function should be a delta function at the w value that corresponds to the dispersion relation as indicated in Figure 21. However, in actuality it is some extended function which represents the convolution of the delta function with a smearing function. The delta function component of $S(k_x, k_y, w)$ comes from a constant magnitude, linearly changing phase, component in $F(k_x, k_y, t)$ which represents the actual wave information that we wish to estimate. The smearing function component of S is the Fourier transform of any modulations of $F(k_x, k_y, t)$ as a function of time beyond the wave information described above. Such modulations represent a multiplicative factor in $F(k_x, k_y, t)$ and thus represent a smearing function in $S(k_x, k_y, w)$.

As discussed in Section 4.2, this modulation function comes from two dominant sources; error in image registration and the SAR MTF. The image registration errors cause only phase errors in $F(k_x, k_y, t)$ since they are shifts in the spatial locations of the original imagery. The MTF modulations cause both phase and magnitude errors in $F(k_x, k_y, t)$. Thus if we plot just the magnitude of $F(k_x, k_y, t)$ for a given (k_x, k_y) location, the modulations will be dominated by the SAR MTF.

The cause of these SAR MTF modulations is illustrated in Figure 22. For each SAR image, the azimuth and range axes are rotated differently due to the nature of spotlight data collection. Thus after performing the two-dimensional Fourier transform, although the k_x, k_y axes are in the same orientation, the MTF spectral coordinates (i.e. range and azimuth wavenumber) are rotated as indicated in Figure 22. This means that modulations in $|F(k_x, k_y, t)|$ for a given (k_x, k_y) are equivalent to modulations along an

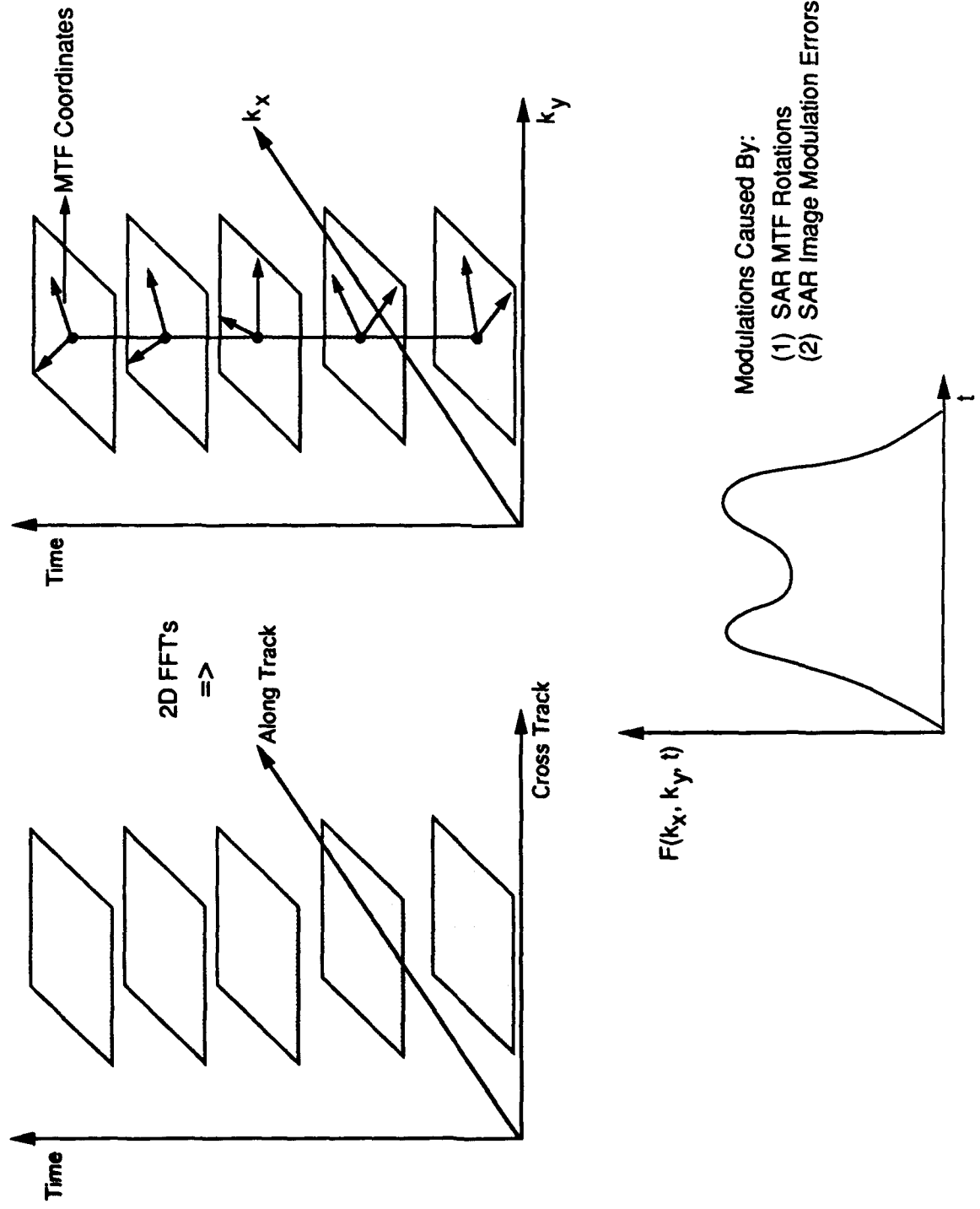


Figure 22. Schematic Showing How Rotation of MTF Determines the Weighting of the Intensity of Image Spectra Versus Time.

angular cut through the magnitude of the SAR MTF. If we let k be the wavenumber for the given spectral location so that $k = \sqrt{k_x^2 + k_y^2}$, then at a specific time t the weighting applied to $F(k_x, k_y, t)$ from the MTF will be the MTF evaluated at the spectral locations $k_x' = k \cos[\Psi + \theta_t]$ and $k_y' = k \sin[\Psi + \theta_t]$ where Ψ is $\tan^{-1}[k_y/k_x]$, the angle of the current spectral location, and θ_t is the rotation of the range and azimuth axes at time t .

The only other dominant modulations in $|F(k_x, k_y, t)|$ are caused by SAR image modulation errors as indicated in Figure 22. We have minimized these however by removing the two-dimensional antenna pattern as discussed above, and additionally by scaling each image separately so that its mean value is one.

Thus a plot of intensity values of the Fourier transform of the SAR images at a given (k_x, k_y) location should have a modulation that is equivalent to the modulation along an angular cut through the SAR MTF. The wavenumber of this angular cut is the same as the wavenumber for the (k_x, k_y) location. The angle of this cut is the squint angle for the data as discussed above.

Such a measurement is shown for the middle altitude case (pass 14) and the high altitude case (pass 15) in Figure 23. Plots both through the dominant wave peak (solid line), at $k=0.07$, and an average over 2 by 2 spectral samples around the dominant peak location (dashed line) are shown. For pass 28 these are essentially equivalent whereas for pass 14 they differ somewhat at the large squint angles. In the analysis below we will not include these large squint angles, so this discrepancy will not effect us. We will use the 2 X 2 averaged data since it has less noise than the dominant wavelength plot.

If the modulations shown in Figure 23 are caused by the SAR MTF, we should be able to fit the parameters of the SAR MTF to this function, and possibly be able to estimate the ranges of those parameters that are consistent with the SAR data. We will utilize a linear version of the MTF as developed in [4] and elsewhere;

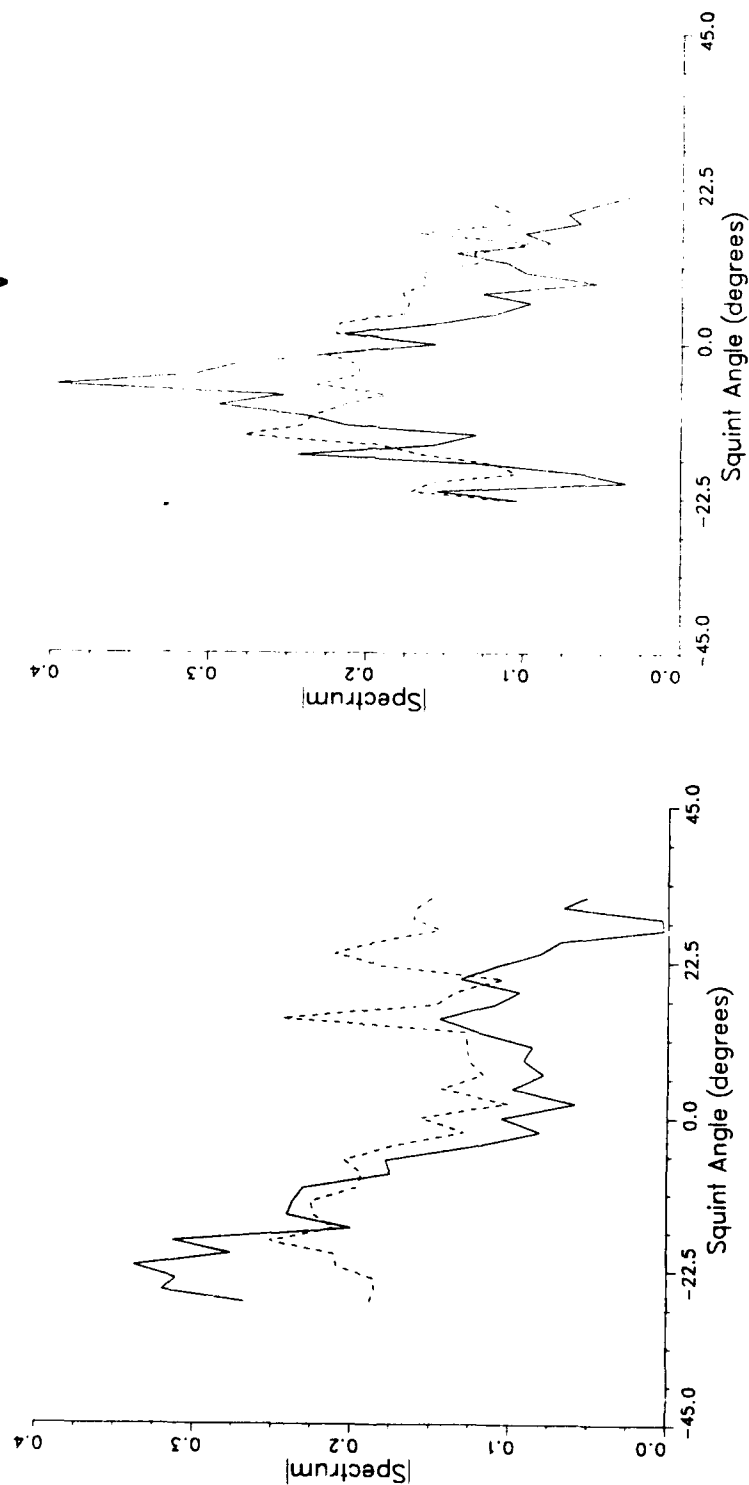
SAXON-FPN SPOTLIGHT SAR SPECTRA

Nov 6



Pass 14 $\theta_1 = 53^\circ \frac{R}{V} = 39-46$

Pass 28 $\theta_1 = 37^\circ \frac{R}{V} = 57-62$



Wavenumbers Averaged

$$\frac{1}{4}$$

Figure 23. Magnitude of SAR Image Spectra Versus Squint Angle (i.e. Time) for Nov. 6 Passes 14 and 28.

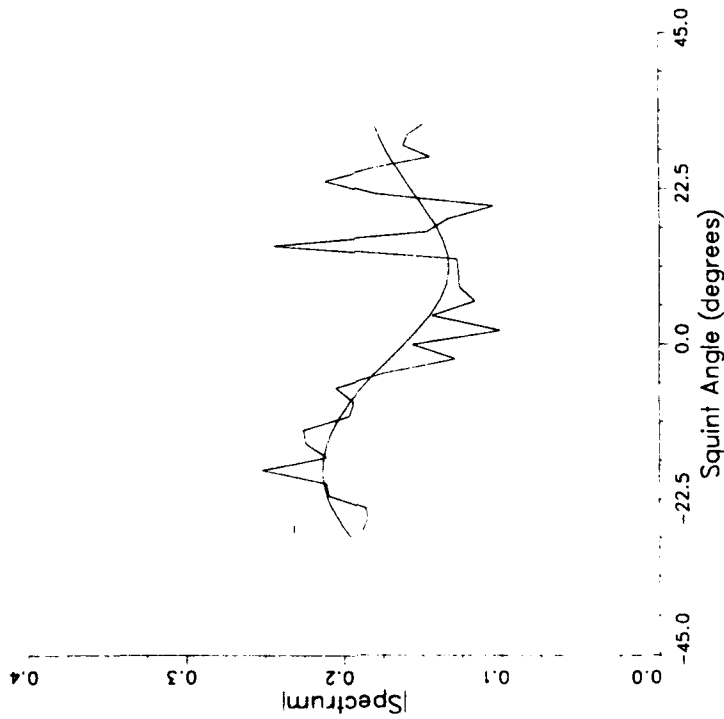
$$MTF(k_x, k_y) = \exp\left[-\frac{1}{2}\left(\frac{R}{V}\sigma_v k_x\right)^2\right] \left(|m| e^{\phi + i \frac{R}{V} w k_x \left[\cos\theta + i \sin\theta \frac{k_y}{k} \right]} \right) \quad (6)$$

where σ_v is the standard deviation of radial velocities, $|m|$ and ϕ are the magnitude and phase, respectively, of the real transfer function (relating wave amplitude to radar cross section), $w = \sqrt{gk}$ and θ is the incidence angle. This linear version is accurate if the last term in Eq. (6) (often called the velocity bunching term) is smaller than 1. Eq. (6) contains three parameters; σ_v , $|m|$ and ϕ that are unknown. We will fit the intensity of Eq. (6) to the SAR data shown in Figure 23 and find the values of the three parameters that minimize the mean squared error between the model and the data. We will allow the MTF to be multiplied by an arbitrary scalar and added to an arbitrary bias term to handle an arbitrary scale factor and a noise floor in the data (although we found that the noise floor in the spectral data was so small that the bias term could be ignored without changing the results).

Figure 24 shows the resulting fit when all the data is used. The values of the three parameters that give this fit are indicated, where positive values for ϕ are locations on the face of the wave pointed toward the sensor. The fit seems very good to the data, however we do know from other measurements the range of values that these parameters should have. The values indicated in Figure 24, especially for σ_v , are significantly outside of that range. One reason for this is the linear MTF model in Eq. (6) actually does not hold for the entire range of squint angles in the data. The velocity bunching term, which must be less than one for this model to hold, depends on k_x . Because these waves are range travelling waves at a squint angle of zero $k_x = 0$. As the squint angle increases k_x subsequently increase. The other parameters in this term, R , V and w , stay constant with squint angle (since wavenumber does not change with squint angle). Thus one can calculate a range of squint angles over which the velocity bunching term is less than some threshold and thus where the linear model in Eq. (6) will be accurate. Using a threshold of 0.5, we calculated that for pass 14 this limits

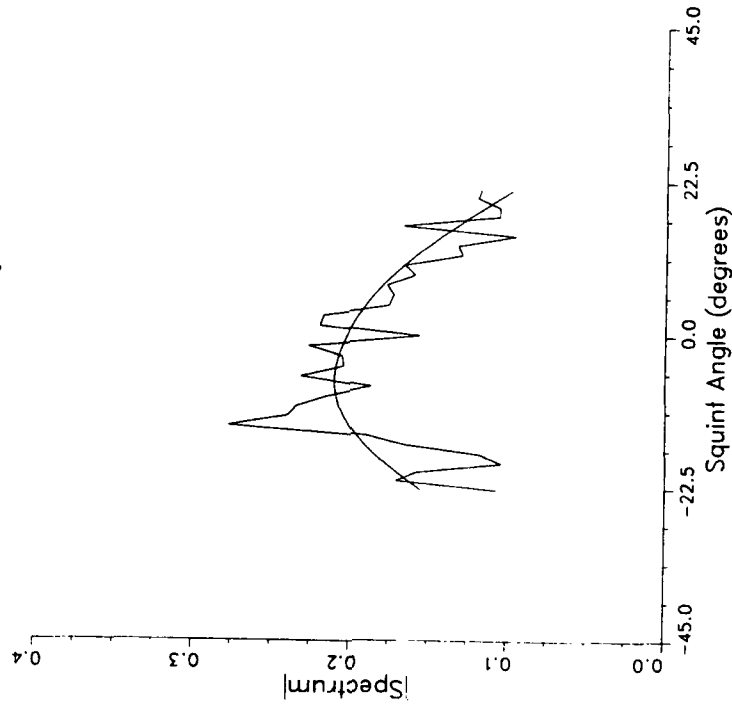
MTF FIT TO FULL SQUINT ANGLE RANGE

Pass 14 $\theta_1 = 53^\circ \frac{R}{V} = 39-46$



$\sigma_V = .8 \quad |m| = 2.4 \quad \phi = 54^\circ$

Pass 28 $\theta_1 = 37^\circ \frac{R}{V} = 57-62$



$\sigma_V = .8 \quad |m| = 9.0 \quad \phi = 34^\circ$

Figure 24. Fit of SAR Data in Figure 23 to Linear MTF Model Across Full Squint Angle Range.

the applicability of Eq. (6) to the squint angle range [-20, 20] degrees and for pass 28 [-14,14] degrees. Note that outside of these ranges the SAR data in Figure 23 shows a significant decrease. It is these downturns that the linear MTF has difficulty modelling. To generate them it must increase the σ_v term so that the exponential in front of Eq. (6) (often called the azimuth fall-off term) generates the required decrease for large squint angles (i.e. large values of k_y). We therefore limited the fitting of the data to these ranges and re-calculated the parameters that minimized the mean squared error. The resulting fits are shown in Figure 25. Note that we have significantly decreased the value of σ_v for pass 28, but not for pass 14. For pass 14 the model is still trying to fit to the slight downturn in the data and thus is requiring a large σ_v value, as can be seen by the slight downturn in the model results for the larger squint angles.

Thus it appears that finding only the minimum fit is not sufficient; there may be other fits with only slightly increase error but with more realistic MTF parameters. To find these, we set the σ_v value at 0.0, 0.1, 0.2, 0.3, 0.4 and 0.5 and found the values of $|m|$ and ϕ_m that minimized the mean squared error, and noted those which still fit the data in Figure 23 to within the noise demonstrated in the data. Similarly we set ϕ_v and $|m|$ to a range of values and found the minimum fit for the other parameters. Using this approach we determined the following ranges for the MTF parameters:

Pass 14: σ_v [0.1, 0.3]

$|m|$ [5, 10]

ϕ [10, 55] degrees

Pass 28: σ_v [0.0, 0.3]

$|m|$ [14, 20]

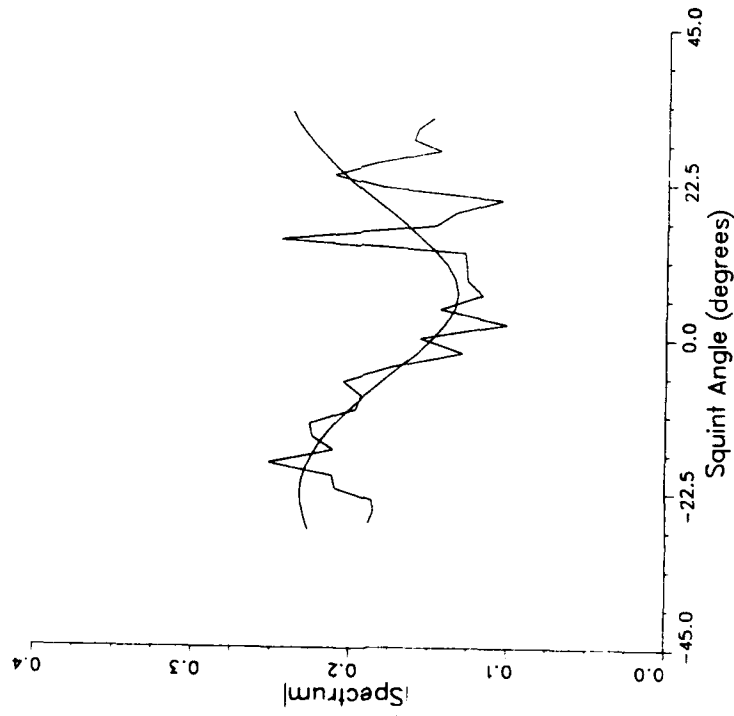
ϕ [-90, 16] degrees.

4.4 COMPARISON TO IN-SITU MEASUREMENTS

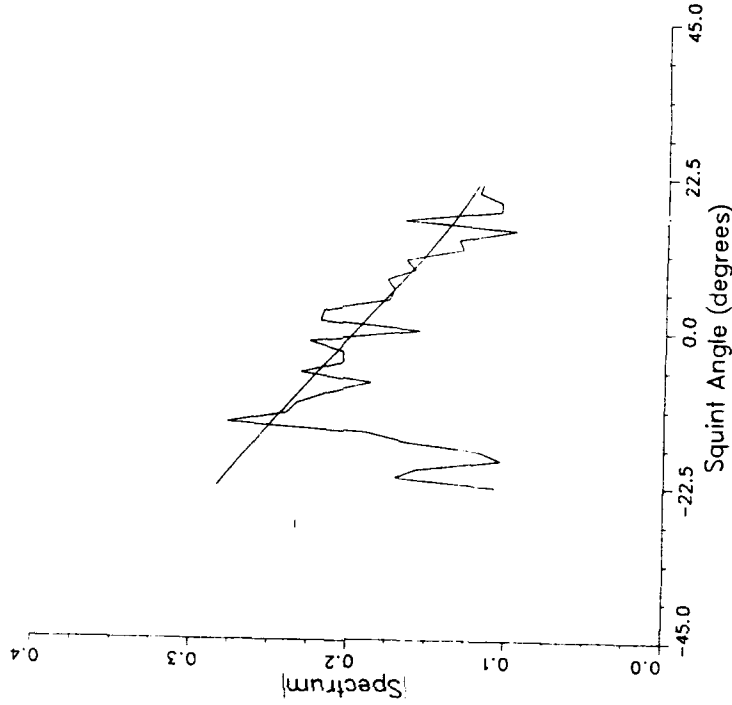
MTF FIT TO LINEAR REGION OF SQUINT ANGLE

$$\text{Pass 14 } \theta_1 = 53^\circ \frac{R}{V} = 39-46$$

$$\text{Pass 28 } \theta_1 = 37^\circ \frac{R}{V} = 57-62$$



$$\sigma_V = 0.7 \quad |m| = 1.7 \quad \phi = -58^\circ$$



$$\sigma_V = 0 \quad |m| = 19.5 \quad \phi = -78^\circ$$

Figure 25. Fit of SAR Data in Figure 23 to Linear MTF Only Over Squint Angle Ranges for Which the Velocity Bunching Term is Less Than 0.5.

5.0 REFERENCES

- [1] Lyzenga, D.R. "Simulation of SAXON-FPN SAR image spectra," Final report for SAXON-FPN program.
- [2] Oliver, C.J. "The interpretation and simulation of clutter textures in coherent images," *Inverse Problems*, 2, 481-518, Nov. 1986.
- [3] Cohen, L., "Time-frequency distributions," *Proc. IEEE*, 77, 941-970, 1989.
- [4] Lyzenga, D.R., "An analytical representation of the synthetic aperture radar image spectrum for ocean waves," *J. Geophys. Res.*, 93, 13859-13865, 1988.

ESTIMATION OF 3-D OCEAN WAVE SPECTRA FROM SPOTLIGHT SAR DATA DURING SAXON-FPN

C.C. Wackerman and D.M. Beverstock

Environmental Research Institute of Michigan
P.O. Box 134001
Ann Arbor, MI 48113-4001

ABSTRACT

SAR spotlight data collected over the ocean surface has the potential of providing three dimensional spectral information. In this paper we discuss two algorithms for estimating these spectra and show their similarities. We also show three dimensional results from data collected during the SAXON-FPN experiment.

1.0 INTRODUCTION

Recently the Synthetic Aperture Radar (SAR) stripmap system that is jointly operated by the Naval Air Warfare Center (NAWC) and the Environmental Research Institute of Michigan (ERIM) has been upgraded to collect spotlight mode data. That is, instead of keeping the antenna aimed orthogonal to the flight path (as in stripmap mode) the antenna is constantly skewed during the collection to keep it focused at one location on the ground. A description of the new mode is given in Section 2 below. One of the advantages of this mode for collections over the ocean is that it provides a series of SAR images of the same ground location at different times, thereby allowing three dimensional (range, azimuth, time) information about the ocean surface waves to be estimated.

For ocean surface waves, the most convenient method of representing this data is the three dimensional spectrum. There are two algorithms for generating spectral estimates from SAR data. The first, which we will call the Short Integration Time Algorithm (SITA) generates SAR intensity images over short integration times where each integration time is centered at a different time value. The resulting two dimensional (range, azimuth) images are then stacked in order of their center times and a three dimensional Fourier transform is taken. The theory that describes this spectral method is discussed in Section 3. The second algorithm, which we will call the Ambiguity Algorithm (AA), lags the raw SAR phase history data for some given range and azimuth intervals and takes a series of two dimensional Fourier transforms for each set of lags. This procedure is identical to calculating the ambiguity function of the phase history data; a tool that has been used for some time by signal processors in analyzing data that varies both spatially and temporally. This theory is discussed in Section 4. As will be shown in Sections 3 and 4 the differences between the two are slight and we will use the SITA in the data analysis of Section 5.

The NAWC/ERIM spotlight system collected ocean wave data during the SAXON-FPN Experiment which took place in the North Sea off of the coast of Germany. The purpose of SAXON-FPN was to understand SAR imaging of ocean surface waves under high wind states and a large amount ground truth air and ocean data was collected on the FPN tower near where the SAR images were taken. In Section 5 we show some spotlight data from this collection and the resulting three dimensional spectral information.

2.0 NAWC/ERIM SPOTLIGHT SYSTEM

The original NAWC/ERIM stripmap SAR is a three frequency (X-, C-, and L-bands) system housed in a P-3A aircraft [1]. In

1990, a spotlight capability was added at L-band where the L-band antenna, instead of being kept orthogonal to the flight path, is rotated in order to keep a specified location on the ground at the center of the beam. The data is recorded the same as in the stripmap mode except that the system is always operated with the smallest possible spacing between range records (0.09 meters) in order to not alias the returns at the largest and smallest look angles. The system is capable of collecting data over look angles from 45 to 135 degrees with a spot size across the entire collection of slightly less than a kilometer in diameter. The illumination pattern is not constant across this spot, but falls off 3-5 dB from peak to edge. The rotation of the antenna is controlled by the motion compensation system of the radar, and thus uncompensated motion can cause the antenna pattern to wander slightly along the ground. These registration errors are estimated in Section 5 below for the SAXON-FPN data. Using nominal collection parameters, this system can record about 40 seconds worth of data in one spotlight pass.

3.0 SHORT INTEGRATION TIME ALGORITHM THEORY

One of the methods used for extracting three dimensional spectra from spotlight data is to stack a series of short integration time images and form the three dimensional Fourier transform. In this section we discuss the theory to describe this output. What follows is a minor modification of [2] to account for the spotlight geometry and the time series of images.

We will denote the data recorded by the SAR, i.e. the raw phase history data, as $s(t, t')$ where t represents slow or azimuth time and t' represents fast or range time. We have that

$$s(t, t') = \iint x(x, y, t) a(x, y) \exp\left[-j \frac{k}{R} (x - vt)^2\right] \exp\left[-j \frac{\gamma}{2(c')^2} (y - c't)^2\right] dx dy \quad (1)$$

where $r(x, y, t)$ is the complex reflectivity of the surface, $a(x, y)$ is the two dimensional antenna pattern, k is the radar wavenumber, R is the range to the surface, γ is the chirp rate of the radar, $c' = c/(2\sin(\theta))$ where c is the speed of light and θ is the incidence angle, x represents azimuth location and y represents range location. Eq. (1) assumes that the surface is frozen during the fast time, t' , but can vary over slow time, t . Also, Eq. (1) assumes that the antenna pattern, $a(x, y)$, is not a function of slow time, and thus we are ignoring any rotations in the pattern during the collection. We will assume that the statistics of the complex reflectivity can be represented as [3]

$$\langle r(x, y, t) r^*(x', y', t + \tau) \rangle = \delta(x - x', y - y') \sigma(x, y, t) \rho(x, y, t, \tau) \quad (2)$$

where the delta function indicates that the reflectivity is spatially uncorrelated, $\sigma(x, y, t)$ is the radar cross section and $\rho(x, y, t, \tau)$ is the normalized temporal correlation function which can be written as

$$\rho(x, y, t, \tau) = \exp\left[\frac{-\tau^2}{2\tau_c^2}\right] \exp\{j2kV_r(x, y, t)\tau\} \quad (3)$$

where the first exponential is the azimuth fall-off effect, τ_x is the correlation time of the surface and $V(x,y,t)$ is the radial velocity of the surface. The complex SAR image, $i(x,y)$, is formed from $s(t,t')$ by a two dimensional correlation where the filter function is set to match the exponentials in Eq. (1). For the spotlight data we will form images using some specified integration time, T_i , centered at some time T . Thus we will index each complex-valued image as $i(x,y,T)$ to indicate what time it corresponds to. We have then that

$$i(x,y,T) = \int_{-T_i/2}^{T_i/2} \int_{-T_i/2}^{T_i/2} s(t,t') w(t-T) \exp\left[i \frac{k}{R} (x-Vt)^2\right] \exp\left[i \frac{Y}{2(c')^2} (y-c't')^2\right] dt dt' \quad (4)$$

where $w(t)$ is equal to 1 for $-T_i/2 \leq t \leq T_i/2$ and zero elsewhere. The intensity image, $I(x,y,T)$ is simply $i(x,y,T)i^*(x,y,T)$. We can now take the three dimensional Fourier transform of $I(x,y,T)$, $F_I(k_x, k_y, w)$, by substituting Eq. (1) into Eq. (4), forming $i(x,y,T)i^*(x,y,T)$ and using the statistics of $r(x,y,t)$ in Eq. (2) to generate

$$\langle F_I(k_x, k_y, w) \rangle = \exp[-i\phi] \frac{\sin(\pi p w)}{\pi w} \iiint \sigma(x,y,t) \rho(x,y,t, \tau_x) a^2(x,y) \exp[-i(xk_x + yk_y + tw)] dx dy dt \quad (5)$$

where $\phi = k_x^2 R / (4k)$, $\tau_x = k_x R / (2Vk)$ and $p = T_i - k_x R / (2Vk)$. By Eq. (5) $\langle F_I(k_x, k_y, w) \rangle$ is simply the three dimensional Fourier transform of $\sigma(x,y,t)\rho(x,y,t,\tau_x)a^2(x,y)$ weighted by a sinc function in w with a phase term quadratic in k_x . Note that the integration time of each image determines the range of w values as well as the range of k_x values via the sinc weighting since the sinc function must be set equal to 0 if p is negative. In addition, note that the temporal correlation function, ρ , also imposes a limit on k_x via the azimuth fall-off which imposes a limit on τ_x .

Although these equations have been described continuously, SAR spotlight data is always analyzed in discrete form, so all of the integrations will become summations and all of the Fourier transforms will be FFT's. Using the discrete form of Eq. (5) one can see that the sample spacing in w will be $1/T_i$ where T_i is the total time covered by the individual images, the sample spacing in k_x will be $1/L_x$ where L_x is the total length in azimuth of the images, and the k_y spacing will similarly be $1/L_y$ where L_y is the length in range. Also, from the above discussions, the SITA limits the w dimension to $|w| < 1/T_i$ and the k_x dimension to $|k_x| < (2kVT_i)/R$ due to the integration time and $|k_x| < (2kV\tau_x)/R$ due to the azimuth fall-off.

4.0 AMBIGUITY ALGORITHM THEORY

It is well known [2,4,5] that the Fourier transform of conjugated lags of $s(t,t')$ will generate intensity image spectra and thus can be utilized to estimate the three dimensional spectrum. We will define the function $A(\tau_x, \tau_y, k_x, k_y)$ as

$$A(\tau_x, \tau_y, k_x, k_y) = \int_{-T_i/2}^{T_i/2} \int_{-T_i/2}^{T_i/2} s(t,t') s^*(t+\tau_x, t'+\tau_y) \exp[-i(tk_x + t'k_y)] dt dt' \quad (6)$$

This is the well known ambiguity function [6] applied to the SAR phase history data. Substituting in Eq. (1) and using the statistics in Eq. (2) one can show that the expected value of Eq. (6) is zero unless $k_x = \gamma\tau_x$, making the ambiguity function essentially three dimensional such that

$$\langle A(\tau_x, \tau_y, k_x) \rangle = \exp[i\phi] \iiint \sigma(x,y,t) \rho(x,y,t, \tau_x) a^2(x,y) \exp[-i(xk_x + yk_y + tw)] dx dy dt \quad (7)$$

where $\phi = (kV^2\tau_x^2)/R + (\gamma\tau_x^2)/2$, $k_x = (2Vk\tau_x)/R$, $k_y = (\gamma\tau_x)/c'$ and $w = k_x - (2V^2k\tau_x)/R = k_x - V k_x$. From Eq. (7) we can see that the k_x axis is limited by the azimuth fall-off in ρ similar to the SITA, but that the integration time limit is not present. Also we can see that the $w=0$ axis drifts along the k_x axis with a slope = V , but there is no limit to the range of w values that there was in the SITA. Following the previous section we can use the discrete version of Eq. (8) to determine that the resulting sample spacing in k_x is $(2Vk\Delta t)/R$ where Δt is the sample spacing in azimuth time of the original phase history, the sample spacing of k_y is $(\gamma\Delta t)/c'$ where $\Delta t'$ is the original phase history sample spacing in the range direction and the sample spacing in w is $1/T_i$ where T_i is the total azimuth phase history time used to calculate the FFT in Eq. (6).

Thus using Section 3 and 4, one can compare the SITA and AA outputs. Both techniques are identical in the range direction. If the same piece of raw phase history data is used for each algorithm, then both have the same w sample spacing, but the SITA has an additional cut-off in w due to the integration time. Both algorithms have a cut-off in k_x due to the azimuth fall-off effect, but the SITA has an additional cutoff due to the integration time; although this is only important for very small integration times. Finally, the two algorithms differ in the k_x sample spacing, with the AA having a slight smaller spacing for nominal operating parameters of the NAWC/ERIM SAR.

There are however significant implementational differences. We have not discussed the range migration problem in this paper, but for the AA it will limit the useful range of phase history data unless the data is corrected for it; a computationally complex procedure. This does not pose a problem in the SITA since it is only the range migration within each image's integration time that is important and (1) these will be short so as not to limit the useful range of w , and (2) most SAR image formation processors already handle range migration. In addition, Sections 3 and 4 have shown that the three dimensional Fourier transform of $\sigma(x,y,t)\rho(x,y,t,\tau_x)a^2(x,y)$ is generated, whereas what is really wanted is the three dimensional Fourier transform of the ocean wave height function. Correcting SAR intensity spectra to estimate wave height spectra is a long known and worked out procedure [7] whereas applying this correction to SAR phase history data is not yet developed. Thus in the analysis of the SAXON-FPN data described in the next section we will limit ourselves to the SITA algorithm.

5.0 SAXON-FPN SPOTLIGHT DATA

We have concentrated on data collected on Nov. 6 where the wind speed was approximately 9.8 m/s and thus the dominant wave will have a period of approximately 8 seconds and a wavelength of approximately 100 meters. To adequately sample the w axis, and thus to avoid significant effects from the sinc weighting in Eq. (5), we generated SAR intensity images that had a 1.54 second integration time and that were spaced by 1.54 seconds. The images were flattened to remove $a(x,y)$ and remapped into the ground plane with a sample spacing of 2.16 meters in both range and azimuth. The extent of the images in both dimensions was 553 meters. Figure 1 shows an example image taken slightly off of broadside with a look angle of 110 degrees and Figure 2 shows its spectrum which has been smoothed slightly to decrease the noise. The concentric circles in the spectrum represent changes in wavelength of 100 meters starting at 500 meters. Note the dominant wavelength is approximately 100 meters and that the waves are dominantly range travelling.

As mentioned above, uncompensated motion in the SAR platform can cause the antenna pattern to wander on the ground. More seriously however, it will also cause an error in positioning the individual images relative to each other; i.e. it will cause a shift in range and azimuth between the images. To estimate this error, we also examined a spotlight pass containing the FPN tower and noted how much the tower shifted from image to image. A maximum error of 4 meters in range and 20 meters in azimuth was estimated over the collection. This amount of jitter represents only a slight smearing of the final 3-D spectrum, so we did not compensate for it.

To generate 3-D spectra of the surface wave height, as opposed to the SAR radar cross section modulation, we need to remove the SAR Modulation Transfer Function (MTF) from each image [7]. This is done by forming the complex-valued Fourier transform of each intensity image, removing the speckle contribution, dividing by the MTF, then inverse Fourier transforming to generate a wave height image. Work is ongoing to fit the MTF environmental parameters that minimize the spectral changes between spotlight images, but for the results of this paper the MTF effects are still present.

Figure 3 shows the results of performing a 3-D Fourier transform on 16 consecutive spotlight images. For each resulting value of w the k_x, k_y data was integrated over angle to form a 1-D function of $k = \sqrt{k_x^2 + k_y^2}$. Figure 3 shows a cascade plot of each of the 1-D curves labelled as to its w value. Note that for a wavelength of 100m ($k = .06$ rad/m) Figure 3 shows a peak at a period of 8 seconds ($w = .79$ rad/s); consistent with the dispersion relation. Also consistent with the dispersion relation is the width of the peaks along the k axis as well as the shift in peaks with w . Figure 3 also indicates some significant stationary clutter at $w=0$. Work is ongoing to use these techniques to separate moving from non-moving clutter.

ACKNOWLEDGMENTS

This work is supported by ONR under Contract N00014-91-C-0207. The technical monitor is Dr. Frank Herr.

REFERENCES

- [1] Sullivan, R., et al., Polarimetric X/L/C-band SAR, *Proceedings of the 1988 IEEE National Radar Conference*, pp. 9-14, Ann Arbor, MI, 1988.
- [2] Lyzenga, D.R., *An analytical representation of the synthetic aperture radar image spectrum for ocean waves*, *J. Geophys. Res.*, **93**, 13859-13865, 1988.
- [3] Hasselmann, K., et al., *Theory of synthetic aperture radar ocean imaging: a MARSEN view*, *J. Geophys. Res.*, **90**, 4659-4686, 1985.
- [4] Hasselmann, K., *A simple algorithm for the direct extraction of the two-dimensional surface image spectrum from the return signal of a synthetic aperture radar*, *Int. J. Remote Sens.*, **1**, 219-240, 1980.
- [5] Martin, P.J., *Direct determination of the two-dimensional image spectrum from raw synthetic aperture radar data*, *IEEE Trans. Geosci. Remote Sens.*, **GE-19**, 194-203, 1981.
- [6] Cohen, L., *Time-frequency distributions*, *Proc. IEEE*, **77**, 941, 1989.
- [7] Monaldo, F.M. and D.R. Lyzenga, *On the estimation of wave slope- and height-variance spectra from SAR imagery*, *IEEE Trans. Geosci. and Remote Sens.*, **GE-24**, 543-551, 1986.

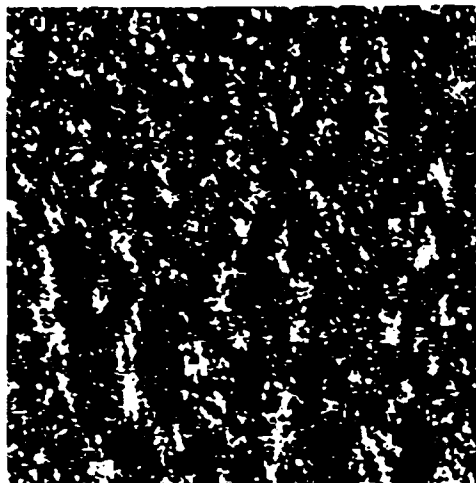


Figure 1. Example spotlight image of SAXON-FPN data taken at a look angle of 110 degrees.

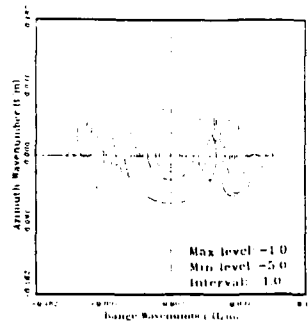


Figure 2. Spectrum of image in Figure 1. Note that the waves have a dominant wavelength of 100 meters and are range travelling.

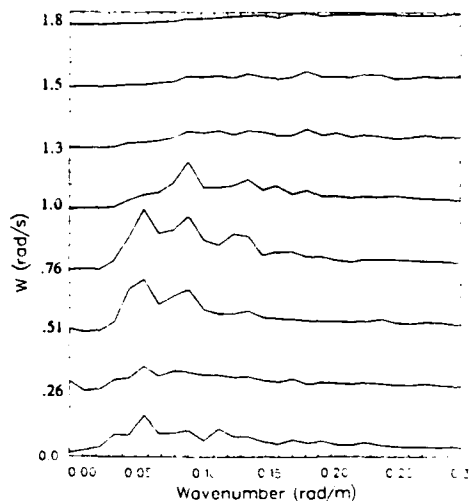


Figure 3. Cascade plot showing the results of 3-D Fourier transform. Each plot is k_x, k_y spectrum integrated over angle for each w value. The (w, k) peak is consistent with the dispersion relation.